Limited earthquake interaction during a geothermal hydraulic stimulation in Helsinki, Finland

Grzegorz Kwiatek[1], Patricia Martínez-Garzón[1], Jörn Davidsen[2,3], Peter Malin[4], Aino Karjalainen[5], Marco Bohnhoff[1,6], and Georg Dresen[1,7]

1. Section 4.2 Geomechanics and Scientific Drilling, Helmholtz Centre Potsdam, GFZ German Research Centre for Geosciences, Potsdam, Germany.
2. Complexity Science Group, Department of Physics and Astronomy, University of Calgary, Canada.
3. Hotchkiss Brain Institute, University of Calgary, Canada.
4. ASIR Advanced Seismic Instrumentation and Research, Dallas, TX, USA
5. St1 Oy, Helsinki, Finland
6. Department of Earth Sciences, Institute of Geological Sciences, Free University Berlin, Berlin, Germany
7. Institute of Earth and Environmental Science, University of Potsdam, Potsdam, Germany

Corresponding Author:

Grzegorz Kwiatek, Section 4.2 Geomechanics and Scientific Drilling, Helmholtz Centre Potsdam, GFZ German Research Centre for Geosciences, Potsdam, Germany, email: kwiatek@gfz-potsdam.de

Abstract

We investigate induced seismicity associated with a hydraulic stimulation campaign performed in 2020 in the 5.8 km deep geothermal OTN-2 well near Helsinki, Finland as part of the St1 Deep Heat project. A total of 2,875 m^3 of fresh water was injected during 16 days at well-head pressures <70 MPa and with flow rates between 400-1000 l/min. The seismicity was monitored using a high-resolution seismic network composed of 10 borehole geophones surrounding the project site and a borehole array of 10 geophones located in adjacent OTN-3 well. A total of 6,121 induced earthquakes with local magnitudes $M_{\mathrm{L}}^{\mathrm{Hel}} > -1.9$ were recorded during and after the stimulation campaign. The analyzed statistical parameters include magnitude-frequency *b*-value, interevent time and interevent time ratio, as well as magnitude correlations. We find that the *b*-value remained stationary for the entire injection period suggesting limited stress build-up or limited fracture network coalescence in the reservoir. The seismicity during the stimulation neither shows signatures of magnitude correlations, nor temporal clustering or anticlustering beyond those arising from varying injection rates. The interevent time statistics are characterized by a Poissonian time-varying distribution. The calculated parameters indicate no earthquake interaction. Focal mechanisms suggest that the injection activated a spatially distributed network of similarly oriented fractures. The seismicity passively responded to the hydraulic energy input rate, with the cumulative seismic moment proportional to the cumulative hydraulic energy and maximum magnitude controlled by injection rate. The performed study provides a base for implementation of time-dependent probabilistic seismic hazard assessment for the project site.

Plain Language Summary

We investigate anthropogenic seismicity associated with fluid injection into the 5.8 km deep geothermal OTN-2 well near Helsinki, Finland, as a part of St1 Deep Heat Project. A total of 2,875 m3 of fresh water was injected during 16 days at well-head pressures <70 MPa and with flow rates between 400-1000 l/min. The seismicity was monitored using a seismic network composed of 20 borehole geophones located in Helsinki area and in the OTN-3 well located close by the injection site. A total of 6,121 earthquakes indicating fractures of 1-30m size were recorded during and after stimulation campaign. Using a handful of statistical properties derived from earthquake catalog we found no indication for earthquakes being triggered by other earthquakes. Instead, the seismicity was found to passively respond to fluid injection campaign, with the earthquake activity rates, as well as the maximum earthquake size being proportional to the fluid injection rate. The spatio-temporal behavior of seismicity and its properties suggest earthquakes occurred not on a single fault, but in a distributed network of similarly oriented fractures. The performed study provides evidence that the induced seismicity due to injection performed within St1 Deep Heat project is stable and allow to constrain seismic hazard.

Keywords

Induced seismicity, hydraulic stimulation, earthquake clustering, earthquake interactions, Poissonian distribution, magnitude correlations, interevent times

Key Points (140 characters each)

1. Induced seismicity associated with stimulation campaign in a 5.8km deep geothermal OTN-2 well passively responds to injection operations

3. Seismicity is a non-stationary Poisson process with seismicity rate and maximum magnitude modulated by the hydraulic energy input rate

4. Seismicity clusters in space and time in response to fluid injection but no interaction between earthquakes is observed

1 Introduction

Seismic hazard associated with fluid injection in the subsurface requires much better understanding of the factors governing the seismic energy release in response to the injection protocol (injection rate, injection pressure, hydraulic energy) and local site conditions (fault inventory, state of stress, local geology). Recently developed models provide an estimate of maximum earthquake magnitude related to fluid injection for a stable, pressure-controlled phase of fluid injection. McGarr (2014) proposed that total seismic moment release and maximum event magnitude increase linearly with total volume of fluid injected, $M_0^{\max} \propto V^1$, $\sum M_0 \propto V^1$, or alternatively to the *volume of rock mass perturbed by fluid injection* $V^{\text{perturbed}}$ and average pore pressure increase in that volume, $M_0^{\max} \propto V^{\text{perturbed}} \Delta P$ (cf. Kwiatek et al., 2015; Martínez-Garzón et al., 2020). The fracture mechanics-based model of Galis et al. (2017) provided estimates of the maximum magnitude of self-arrested ruptures increasing nonlinearly with total fluid volume, $M_0^{\max} \propto V^{3/2}$. Using the seismogenic index concept (e.g. Shapiro et al., 2010), van der Elst et al. (2016) related injected fluid volume to seismic activity, total seismic moment release and maximum magnitude, with $M_0^{\max} \propto V^{3/2}$ for a Gutenberg-Richter *b*-value of 1. Based on a recent conceptual model (Lord-May et al., 2020) one can generalize the relation between injected fluid volume, magnitude-frequency distribution and resulting seismic hazard, which depends on the loading history arising from both fluid injections and natural aseismic loading as well as on the heterogeneity of the host medium.

Most of the proposed models of increasing $M_0^{\max}$ with injected V are limited to a stable, pressure-controlled regime but do not capture a potential transition to an *unstable* or *runaway* rupture (see e.g. discussion in Kroll and Cochran, 2021). Such an unstable event may affect the entire length and width of tectonic faults within or near the stimulated reservoir. Bentz et al. (2020) compiled numerous studies of fluid-induced seismicity and showed that most of the analyzed enhanced geothermal systems displayed a prolonged, stable period of seismic energy E_0 (or seismic moment M_0) release in response to fluid injection. This stable period was observed irrespective of varying seismic injection efficiencies η^{inj}, where η^{inj} is the ratio of seismic E_0 to hydraulic energy E_H (e.g. Maxwell, 2011). In general, the estimated radiated seismic energy of the studies analyzed by Bentz et al. (2020) remained below the maximum event magnitude predicted by the McGarr (2014) model.

Increasing total seismic energy release with total fluid volume was also found in laboratory experiments (Wang et al., 2020a, 2020b). In contrast to a stable evolution of seismic moment observed for most projects, others displayed seismic moment evolution with progressive injection clearly indicating an unstable energy release. Examples include the Pohang EGS (c.f. Ellsworth et al., 2019)

and Cooper Basin EGS (c.f. Baisch, 2020) displaying continuously increasing η^{inj} throughout the injection periods, representing a signature of an emerging failure process leading to *runaway* rupture.

The transition towards unstable failure in an otherwise *stable*, pressure-controlled regime is not well understood. The physical mechanisms governing a transition from a stable injection regime into a run-away rupture are still a matter of debate (Wang et al., 2020a, 2020b). This transition could be governed by total injected fluid volume (Galis et al., 2017) or pressure build-up and injection rate (Alghannam and Juanes, 2020; Rudnicki and Zhan, 2020; Wang et al., 2020a, 2020a). Site conditions, including background stress level and its orientation with respect to a local fault or fault network, in addition to elevated pore fluid pressures may promote stress transfer between events (earthquake interactions, aftershock or triggering processes, see e.g. Cochran et al., 2020; Verdeccia et al., 2021 and references therein for details). That is to say that there are several critical factors that may contribute to induced seismic activity and the occurrence of large earthquakes.

It is still a matter of debate to what extent earthquake interaction affect the evolution of induced seismicity activity. A fluid-induced and pressure-controlled earthquake sequence may be modelled by a random *Poisson* process (e.g. Langenbruch et al., 2011), where successively occurring events are not causally related to each other ('background seismicity'). The observed total number of seismic events as well as seismicity rates can be successfully reproduced assuming a fluid pressure perturbation and free model parameters such as friction or cohesion (Gischig and Wiemer, 2013). In contrast, Catalli et al. (2013, 2016) showed that static stress transfer between induced earthquakes may in fact play a significant role in triggering earthquakes in EGS stimulation campaigns, especially towards the end of injection. Schoenball et al. (2012) investigated seismicity recorded in the Soultz-sous-Forets EGS project. They found that static stress changes may vary considerably on a local scale, promoting local earthquake interactions. This agrees with analysis of acoustic emission events during rock deformation laboratory stick-slip experiments, where local stress concentrations caused by defects (inclusions, notches), rather than global stress level, were found to control event-event triggering (Meredith and Atkinson, 1983; Davidsen et al., 2021). Schoenball et al. (2012) found that triggering by static stress transfer plays a minor role in reservoirs for which deformation is distributed over a certain volume, but may lead to interacting events within a single and prominent fault zone. Martínez-Garzón et al. (2018) studied the clustering and triggering properties of three geothermal reservoirs in California, USA. They found increased earthquake triggering during periods of high injection rates (i.e. stressing rates). They also noted that reservoir structure and ambient stress state affected the rate of background seismicity. Yeo et al. (2020) studied seismicity associated with fluid injection in Pohang, South Korea. They found that cumulative Coulomb stress changes from small earthquakes on a single fault are in the range of stress changes due to pore pressure changes, suggesting that that large

induced events may drive seismicity leading to the occurrence of large earthquakes. Finally, Catalli et al. (2016) and Brown and Ge (2018) highlighted the importance of stress transfer between seismic events for earthquake forecasting and seismic hazard assessment. Brown and Ge (2018) recommended mitigation actions if seismic analysis indicates stress transfer and triggering, in particular in the absence of fluid injection.

In June-July 2018, a total volume of 18,160 m^3 of water was injected into the crystalline basement during a first stimulation campaign performed in the St1 Deep Heat project in Helsinki, Finland (Ader et al., 2019; Kwiatek et al., 2019; Hillers et al., 2020; Leonhardt et al., 2021b). The injection schedule was adopted in a feedback traffic light-system in response to near-real-time seismic monitoring of induced seismicity rates, hypocenter locations and magnitudes, and evolution of seismic and hydraulic energy (Kwiatek et al., 2019). This adaptive stimulation approach allowed to avoid the occurrence of a „red alert" seismic event with a moment magnitude above M_W 2.0, which was a limit set by the local authorities.

In this study we analyze the induced seismicity associated with a follow-up stimulation campaign performed in May 2020 (Rintamäki et al., 2021). We first develop a high resolution seismicity catalog and then analyze the seismic activity in response to the injection operations in 2020 and compare it to the previous massive stimulation campaign in June-August 2018 (e.g. Kwiatek et al., 2019).We calculate statistical and spatio-temporal properties of the induced seismicity in response to injection operations performed at the site, with a special focus on parameters signifying potential earthquake interactions. We then discuss the implications of our observations for local seismic hazard. Our study highlights that high-frequency low-magnitude monitoring and near-real-time analysis of seismic data, combined with analysis of the reservoir structure and local stress conditions are prerequisite in attempts to successfully control induced seismicity in the St1 Deep Heat project and other comparable deep geothermal systems.

2 Data and methods

Project site

The St1 Deep Heat project site is located on the Aalto University campus in Helsinki, Finland. (**Figure 1**) (Kwiatek et al., 2019). Two deep injection wells (OTN-2, OTN-3) were drilled into Precambrian basement rocks. The deeper well OTN-3 reached 6,400 m measured depth (6,087 m b.s.l., 6,100 m of overburden) with an open- hole section of 1,000 m inclined at 45° towards NE (Fig. 1b-c). The well was stimulated in June and July 2018 (Ader et al., 2019; Kwiatek et al., 2019; Hillers et al., 2020; Leonhardt et al., 2021b). Between late 2019 and Spring 2020, the existing shallower well OTN-2 was deepened to the final depth of 5,765 m b.s.l. with a deviated bottom hole section parallel to the OTN-3 trace. Open-

hole sections of both wells are separated laterally by approx. 400 m. Azimuths of both wells are approximately perpendicular to the direction of maximum horizontal stress.

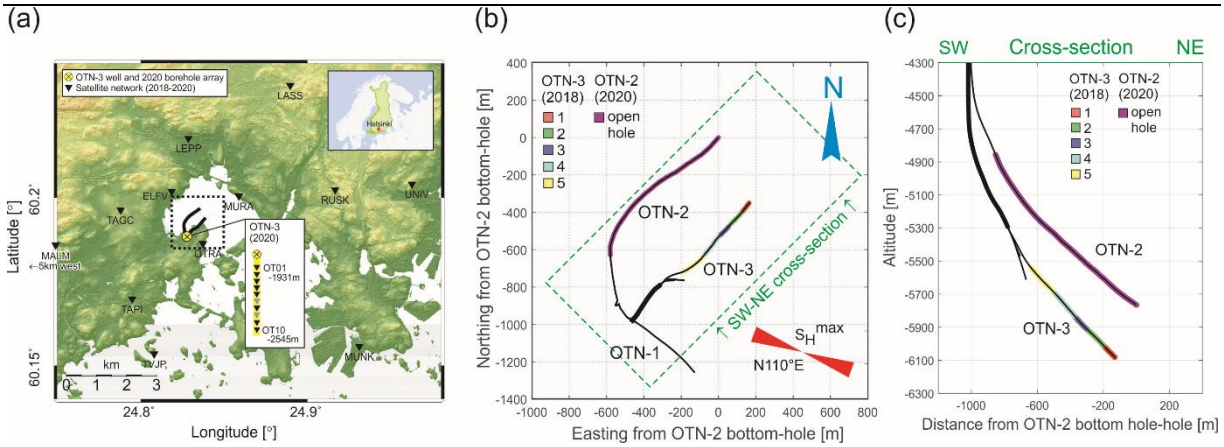

Figure 1. (a): Overview of the St1 Deep Heat project site in Helsinki/Finland and the status of the downhole seismic monitoring network during the 2020 OTN-2 stimulation. Black reverted triangles denote individual borehole geophones (depth range 238-1,133 m b.s.l.) and slots of a vertical array in the well OTN-3 (depth range 1,931-2,545m b.s.l.). Grey sensors within the vertical array were not used in analysis due to enhanced electronic noises; (b): Zoom-in of the dotted rectangle in (a). The 2020 open-hole stimulation interval in the OTN-2 well is shown in magenta. Depth intervals in OTN-3 hydraulically stimulated in 2018 are encoded by five different colors (see Kwiatek et al., 2019 for details); (c): SW-NE depth section seen from SE focused on lowermost portions of the OTN-2 and OTN-3 wells.

OTN-2 stimulation campaign in May 2020

Between May 4th, 2020 and May 20th, 2020, a total of 2,875 m^3 of water were injected into the open-hole section of the OTN-2 well in the depth interval 4856-5765 m b.s.l. (Fig. 1b-c) (Rintamäki et al., 2021) to establish communication between two wells. Similar to the 2018 stimulation campaign performed in well OTN-3, the 2020 stimulation was flow-rate controlled. The maximum well head pressures did not exceed 70 MPa and injection rates were kept at a relatively low level of 400 l/min (during 84% of the injection period), with occasional short periods of injection at rates up to 1,000 l/min (**Figure 2**). The total volume of fluid injected was only about 16% of the 18,000 m^3 injected in 2018. Well head pressures also were substantially below the maximum 90 MPa reached in 2018 (c.f. Kwiatek et al., 2019).

Seismic Monitoring

The near-real-time seismic monitoring network of the 2020 stimulation campaign at OTN-2 was composed of 24 borehole geophones. The centerpiece was a 10-level borehole array (hereafter called "borehole array") of Geospace OMNI-2400 geophones (3-components, 15 Hz natural frequency) sampled at 2 kHz. Compared to the instrumentation used to monitor the 2018 stimulation, the

borehole array was modified by removing two sensors and increasing the spacing between the remaining 10 sensors. The refurbished array was placed in the OTN-3 well at 1.93 - 2.55 km depth. This was close to the location of the borehole array placed in the OTN-2 well at depths 2.20-2.65 km during the campaign in 2018 (see inset in Fig. 1a). Additional 12 stations (hereafter called “satellite network”) equipped with short-period 3-component 4.5 Hz natural frequency Sunfull PSH geophones completed the monitoring network. The geophones were installed before the 2018 stimulation campaign (Fig. 1a) in 0.30 - 1.13 km deep wells surrounding the injection well extending throughout the Helsinki area. The entire monitoring system was fully operational in Dec 2019, about 5 months before the May 2020 stimulation.

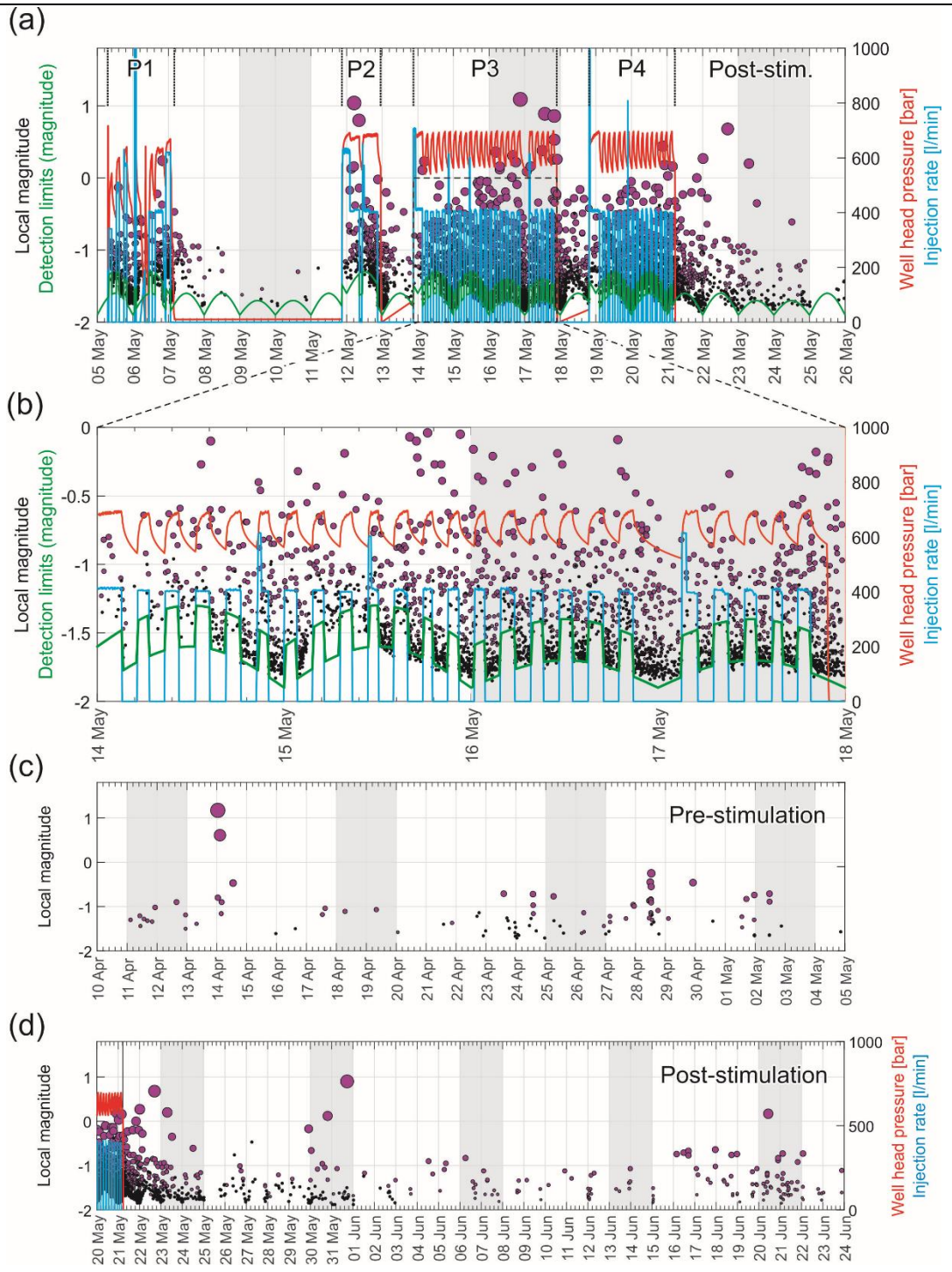

Figure 2. (a): Overview of hydraulic and seismicity parameters for the 2020 OTN-2 stimulation campaign in May 2020. Circles represent local magnitude of detected seismic events. The red and blue solid lines correspond to the OTN-2 well head pressure and injection rate, respectively. Selected time intervals of the injection campaign are labelled P1-P4 and the empirically derived fit to the limits to earthquake detection limit is shown by the green solid line (see text for detailed discussion). (b): Zoom-in of time period between May 14th and May 18th days during injection phase P3 of the injection campaign showing fluctuations of the earthquake detection threshold in response to daily urban noise level changes and injection-related noises. Note the slightly improved detection

conditions during the weekend period (shaded days); (c) last weeks of seismicity preceding the OTN-2 stimulation campaign; (d) seismicity following the OTN-2 stimulation campaign.

Near-real-time processing of induced seismicity data started on Jan 26, 2020, i.e. about 3 months prior to the onset of the injection. This provided extensive information on the background seismicity around the injection site used for seismic hazard assessment. The seismic network and near-real-time processing provided a very consistent seismic catalog for this entire period. Monitoring and processing stopped end of June 2020, about one month after the stimulation of the well was completed.

Seismic catalog development

The seismicity catalog provided by the industrial operator initially contained 6,243 event detections including mostly induced earthquakes, but also electronic noises and signals originating from or near the surface. To refine the catalog, we first included additional events (detections) that were only recorded by the deep OTN-3 array. To optimize detections of missing induced seismic events from within the stimulated reservoir, a coincidence trigger was run on the database of remaining *P*-wave arrivals only observed at stations forming the OTN-3 array (see similar procedure applied in Kwiatek et al., 2019; Leonhardt et al., 2021b). This enhanced the initial catalog by 3,720 newly detected events to a total of 9,963 detected events.

Then we performed an automated inspection of observed hodographs by comparing the observed patterns of P- and S-wave arrivals on sensors forming the OTN-3 array with those predicted for events occurring nearby the OTN-2 injection volume (defined as cube of 2×2×2 km^3 centered at the injection interval). This allowed to confirm that 6,318 events out of the 9,963 detected events originate from the stimulated reservoir. The remaining 3,645 events were manually inspected. It turned out they are transient signals of mechanical (low frequency) or electronic (high frequency) origin or seismic events related to surface blasting and soil compaction works performed in well-identified areas surrounding the project site (3-7 km away).

The vast majority of the 6,318 confirmed induced seismic events were only visible on seismograms from sensors forming the OTN-3 array. Using clearly visible P- and S-wave arrivals, the distance between induced earthquakes from OTN-3 array sensors as well as event magnitudes could be well estimated (see next section). Local „Helsinki" (Uski and Tuppurainen, 1996; Uski et al., 2015) magnitudes ranging from $M_{\mathrm{L}}^{\mathrm{Hel}}$ -1.5 to $M_{\mathrm{L}}^{\mathrm{Hel}}$ 1.2 could be then calculated for all 6,318 seismic events. To locate the seismic events, we used the Equivalent Differential Time (EDT) method (Font et al., 2004) as in previous studies (Kwiatek et al., 2019; Leonhardt et al., 2021b). We used a 1D P-wave velocity model based on a vertical seismic profiling campaign (Leonhardt et al., 2021b) assuming a V_P/V_S ratio of 1.71 for inverting S-wave arrival times. The location inverse problem was solved using the

Metropolis-Hastings Random Walk algorithm (MHRW, Metropolis et al., (1953); Hastings (1970). Hypocenter locations (x, y, z) were estimated as mode from MHRW-sampled empirical probability density distributions of hypocenter locations.

However, using the MHRW-derived location uncertainties, we found the accurate hypocentral locations could not be achieved for most events without additional *P*- and *S*- phase arrivals from sensors forming the satellite network. This was evidenced by elongated empirical distributions of location uncertainties obtained from MHRW algorithm suggesting a clear lack of sufficient azimuthal coverage due to lack of picks from satellite network. Consequently, only 72 largest events could be well located using additional P- and S-wave onsets available on sensors forming the satellite network. In the following, these 72 earthquakes were further relocated using the Double-Difference (DD) method (Waldhauser and Ellsworth, 2000). These events and 1,987 events from the earlier 2018 stimulation (Leonhardt et al., 2021a) of well OTN-3 were relocated jointly. The combined relocation of both catalogs allowed preserving the relative distances between all clusters of seismic events forming the 2018 seismicity and new clusters activated during the 2020 stimulation. For the 2020 stimulation we ultimately relocated 45 events out of initial 72. The relative location precision (95% confidence interval) in horizontal and vertical direction was not exceeding ±85 m and ±42 m, respectively.

Local magnitude $M_{\mathrm{L}}^{\mathrm{Hel}}$, **seismic moment** M_0 and **radiated energy** E_0. Local magnitude $M_{\mathrm{L}}^{\mathrm{Hel}}$ was calculated following Uski and Tuppurainen (1996) and Uski et al. (2015) using seven selected sensors from the borehole array that displayed the lowest noises across the full frequency band of the seismic recordings. The magnitude has been converted to seismic moment M_0 following the regressive relation from Uski et al. (2015). The seismic moment was directly converted to radiated seismic energy E_0 (Hanks and Kanamori, 1979):

$$E_0 = \Delta\sigma \frac{M_0}{2G}, \quad [1]$$

assuming a stress drop value of $\Delta\sigma = 9$ MPa and a shear modulus of $G = 39$ GPa (see Kwiatek et al., 2019 for details).

***b*-value.** The slope of the magnitude-frequency distribution of events (*b*-value) and the magnitude of completeness (M_{C}) have been calculated for the seismic catalog using the maximum likelihood method (Utsu, 1965), including a correction for the histogram bin size (Lasocki and Papadimitriou, 2006), and the goodness of fit method (Wiemer and Wyss, 2000). For the latter, we calculated the *b*-value assuming that 95% of the events follow a Gutenberg-Richter power law. To investigate the temporal evolution during injection periods, we additionally calculated the *b*-value in a moving-time

window of 250 events. The uncertainties in *b*-value were estimated following Shi and Bolt (1982) suitable for time varying *b*-values.

Magnitude correlations. For selected time periods we tested whether magnitude correlations exist between consecutive events included in the seismic catalog. Magnitude correlations between events would allow forecasting the magnitude of the pending forthcoming earthquake based on the current seismic catalog (Davidsen et al., 2012; Maghsoudi et al., 2016). In particular, we focused on the observed catalog of magnitude differences,

$$\boldsymbol{\Delta M} = [\Delta M_i] = M_{i+1} - M_i, \quad [2]$$

where $[\Delta M_i]$ is the catalog of earthquake magnitude differences exceeding the magnitude of completeness ordered by time. The Probability Density Function (PDF) of samples, $p(\boldsymbol{\Delta M})$, is expected to significantly deviate from the distribution of magnitude differences $p(\boldsymbol{\Delta M}^*)$ of uncorrelated magnitudes $\boldsymbol{\Delta M}^* = [\Delta \mathrm{M}_i^*]$ if a correlation between the magnitudes of consecutive events would exist (e.g. Davidsen et al., 2012). The latter distribution can be obtained by considering $\Delta M_i^* = M_{i^*} - M_i$, where M_i is the *i-th* magnitude in the original catalog of magnitudes and each M_{i^*} is a magnitude randomly drawn from the original catalog of magnitudes. This vector of uncorrelated magnitudes can be generated multiple times, allowing to quantify the variability of $p(\boldsymbol{\Delta M}^*)$ formed from many series realizations of $[\Delta M_i^*]$. In the following, differences between original cumulative distribution functions (CDFs), $p(\boldsymbol{\Delta M} < \Delta m)$, and CDFs built upon the perturbed vectors of magnitudes are calculated:

$$\delta p(\Delta m) = p(\boldsymbol{\Delta M} < \Delta m) - p(\boldsymbol{\Delta M}^* < \Delta m). \quad [3]$$

In the absence of magnitude correlations, $\delta p(\Delta m)$ should not significantly deviate from 0 for all considered Δm. In contrast, if the probability density function of magnitude differences formed from $\boldsymbol{\Delta M}$ is significantly different from those built upon multiple random permutations of the same catalog, the catalog may display magnitude correlations.

Interevent time statistics. To calculate the interevent time statistics, we started from the ordered sequence of interevent times:

$$\boldsymbol{\Delta T} = [\Delta T_i] = T_{i+1} - T_i, \quad [4]$$

and calculated the corresponding probability density function, $p(\boldsymbol{\Delta T}/\langle \Delta T \rangle)$, where $\langle \Delta T \rangle$ is the mean interevent time of the whole sequence containing *N* elements: $\langle \Delta T \rangle = (T_N - T_1)/(N-1)$.

Interevent time ratio. Following van der Elst and Brodsky (2010) the interevent time ratio statistics were calculated using a temporally-ordered seismicity catalog of selected seismic events $\boldsymbol{T} = [T_i]$:

$$\boldsymbol{R} = [R_i] = \frac{T_{i+1} - T_i}{T_{i+1} - T_{i-1}}. \quad [5]$$

In the absence of temporal (anti-)clustering of seismic events (e.g. aftershock or foreshock sequences), i.e. for a stationary or time-varying *Poisson* process, $p(\boldsymbol{R})$ is expected to be a uniform distribution in the interval [0, 1]. Temporal clustering and anti-clustering of seismicity is expressed by statistically significant peaks of $p(\boldsymbol{R})$ observed around 0 and 1, respectively (van der Elst and Brodsky, 2010). The significance of (anti-)clustering (or deviation from a Poissonian process) can be assessed by comparing the empirical $p(\boldsymbol{R})$ to that built upon the sample of data randomly distributed in time (i.e. following Poisson process) with the same number of events as the empirical catalog (Davidsen et al., 2017, 2021). To strengthen the inference, one can further condition $p(\boldsymbol{R})$ on the magnitude of events (i. e. larger events are expected to trigger more frequently), or on the difference in magnitudes of adjacent events (i.e. larger events preceding the smaller ones signify aftershock sequences). Such conditioning of the dataset should amplify any potential triggering behavior if it exists.

Focal mechanisms. We calculated 14 double-couple constrained moment tensors using the hybridMT moment tensor inversion package (Kwiatek et al., 2016) and time integrals of the first P-wave ground displacement pulses including sign information (e.g. Amemoutou et al., 2021). We performed 200 resampling of the input data by perturbing the take-off angles by up to ±6 degrees to simulate the uncertainties in the velocity model and location (Martínez-Garzón et al., 2017), and we allowed for variation in input amplitudes up to 30% to simulate effects of noise (Davi et al., 2013; Stierle et al., 2014). This sampling procedure aimed to identify focal mechanisms that are insensitive to imposed noise variations and velocity model uncertainties. For each earthquake, the stability of its focal mechanism has been assessed by calculating the 3D rotation angle δ (Kagan, 2007) between best solution and sampled solutions (see similar procedure in Goebel et al., 2017; Dresen et al., 2020). We ultimately selected 8 moment tensor solutions for which the variability of sampled mechanisms did not exceed 20°. Additionally, we calculated full moment tensors obtaining initially low level of the isotropic components (<10%). However, the performed BIC test (Cesca et al., 2013; Bentz et al., 2018) indicated an insignificant improvement of the root-mean-square error between full MT and DC-constrained MT inversion results. Therefore, we decided to use the double-couple constrained moment tensors calculated beforehand.

3 Results

Seismic response to injection operations

Between January 2020 and the start of the stimulation campaign in May 2020 a total of 197 earthquakes were detected originating in the vicinity of the two wells OTN-2 and OTN-3 at >5.0 km

depth. This activity consisted of mostly small seismic events that were likely triggered by engineering operations at the OTN-2 well. A remarkable doublet of well-recorded seismic events with $M_{\mathrm{L}}^{\mathrm{Hel}}$ 1.2 and $M_{\mathrm{L}}^{\mathrm{Hel}}$ 0.6 separated by a few hours occurred on April 14th, 2020 (Fig. 2c). This doublet was preceded by a few smaller events the same day and it was also followed by some activity during the 24 hours following the $M_{\mathrm{L}}^{\mathrm{Hel}}$ 0.6 second event. Other than the two main events, event magnitudes of associated activity were $M_{\mathrm{L}}^{\mathrm{Hel}} < -0.5$ (Fig. 2C) and they showed no accelerating or decelerating (Omori-type) behavior. It is conceivable, that the events were caused by mud replacement operations performed in OTN-2 well. Sparse seismic activity was observed throughout the following two weeks with $M_L^{\mathrm{Hel}} < 0.3$, until the beginning of the injection campaign in OTN-2.

The OTN-2 stimulation started on May 5th, 2020 and lasted nearly 16 days. Active fluid injection was maintained during half (49%) of the entire time period (Fig. 2a). The fluid was injected into the entire OTN-2 open hole section. For technical reasons, the stimulation was separated timewise into four phases (P1-P4 in Fig. 2a) (St1 Oy – pers. comm). Each injection phase resulted in a significant increase in seismic moment M_0 and radiated seismic energy release E_0. Similarly to the 2018 stimulation, the E_0 was found to be closely related to the hydraulic energy input E_H (**Figure 3c**). Hydraulic energy was estimated from:

$$E_H = \int_0^t P(t)V(t)dt, \qquad [6]$$

where P is the wellhead pressure, V is fluid volume and t is time. We found the cumulative seismic energy release to be proportional to the hydraulic energy (Fig. 3c), however, at a slightly lower level of seismic injection efficiency η^{inj} than that observed in 2018.

During the stimulation period a total of 5,427 earthquakes were detected (N=2,494 with $M_{\mathrm{L}}^{\mathrm{Hel}} > M_{\mathrm{C}} = -1.4$) with largest event magnitude $M_{\mathrm{L}}^{\mathrm{Hel}} = 1.1$. The evolution of maximum event magnitudes and cumulative seismic moment release roughly followed the trend predicted by the models of Galis et al. (2017) and van der Elst et al. (2016) (Fig. 3d). Event magnitudes remained way below values predicted by the model of McGarr (2014). The *b*-values for the quasi-stationary injection period during injection phases P2-P4, where the injection rates and pressure were relatively stable, is *b*=1.3±0.1 at a magnitude of completeness $M_C = -1.4$ (Fig. 3a). The observed *b*-values are similar to those from the 2018 stimulation (*b*=1.3, Kwiatek et al., 2019). These *b*-values are common for induced seismicity, but slightly larger than observed for natural earthquakes (*b*=1 on average). Similar to the 2018 stimulation in OTN-3 well, at the beginning of stimulation campaign (P1 in Fig. 2a) we observe slightly higher *b*-values, whereas for the remaining period we did not observe statistically significant temporal changes in the *b*-value (Fig. 3b).

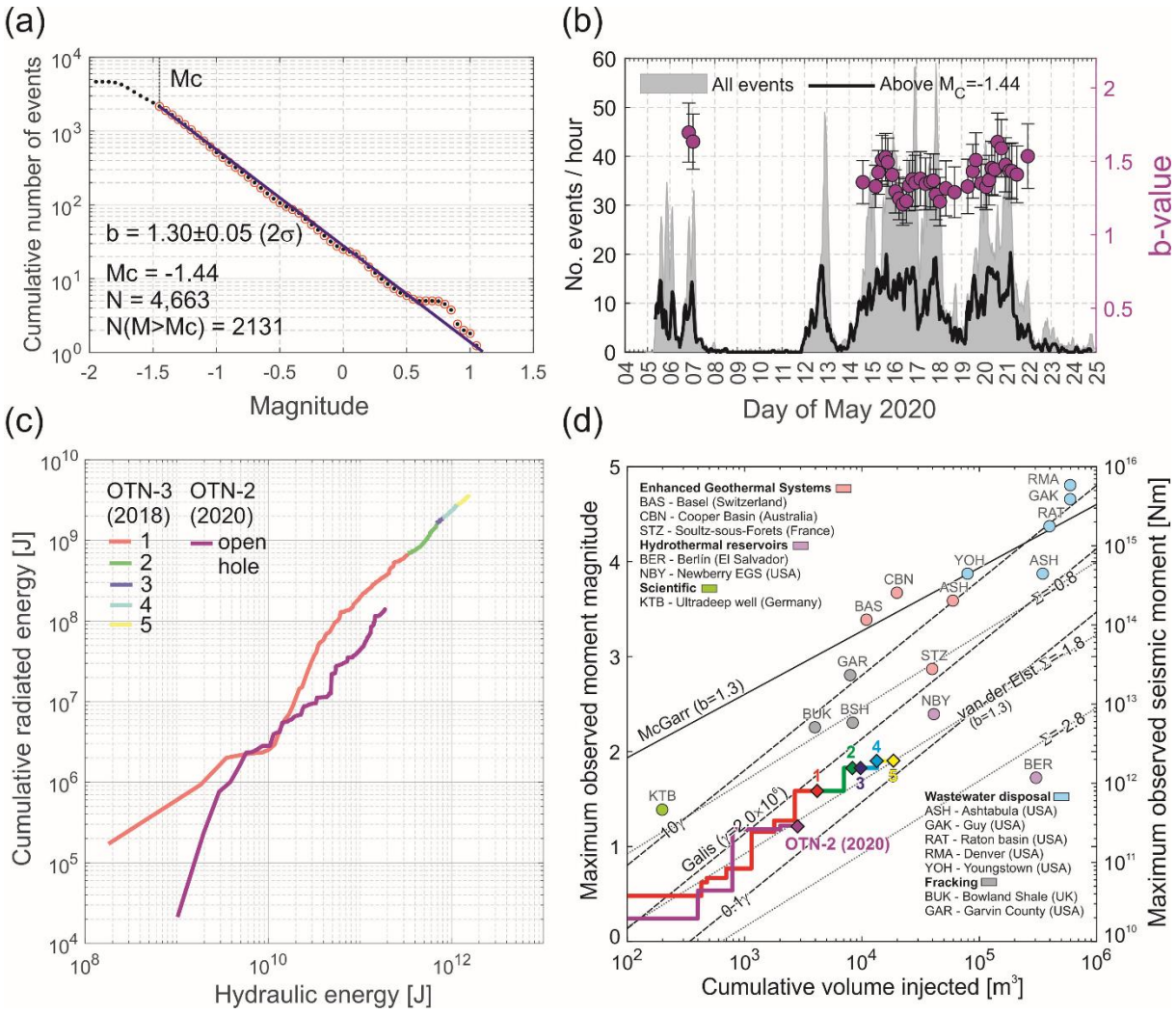

Figure 3. (a): Cumulative frequency-magnitude Gutenberg-Richter distribution calculated for injection phases P2-P4; (b): Temporal evolution of the *b*-value during injection and shortly after injection using a moving window of N=250 events. The vertical error bar corresponds to 2σ error of the b-value estimate; (c): Relation between cumulative hydraulic energy E_{H} and cumulative seismic radiated energy E_0 during the 2018 and 2020 stimulations; (d): Relation between cumulative fluid volume and maximum earthquake magnitude for the 2018 (color reflect phase 1-5 of injection, see Kwiatek et al., 2019 and Leonhardt et al., 2021 for details) and 2020 stimulations (magenta).)

Fluid injection was stopped on May 21st, 2020, but seismic monitoring continued during the shut-in and post-injection phase until Jun 23rd, 2020 recording 694 earthquakes in total. For the first four days of the post-injection period we observed a rapid decline in seismic activity (Fig. 2a), followed by a gentler decline of seismic activity (Fig. 2d). Small bursts of seismic activity occurred at the end of the monitoring period, likely related to technical operations in the OTN-2 borehole following shut-in of the

well. The observed maximum magnitude after shut-in reached $M_{\mathrm{L}}^{\mathrm{Hel}}$ 1.0 and occurred 10 days after injection (Fig. 2d) stopped.

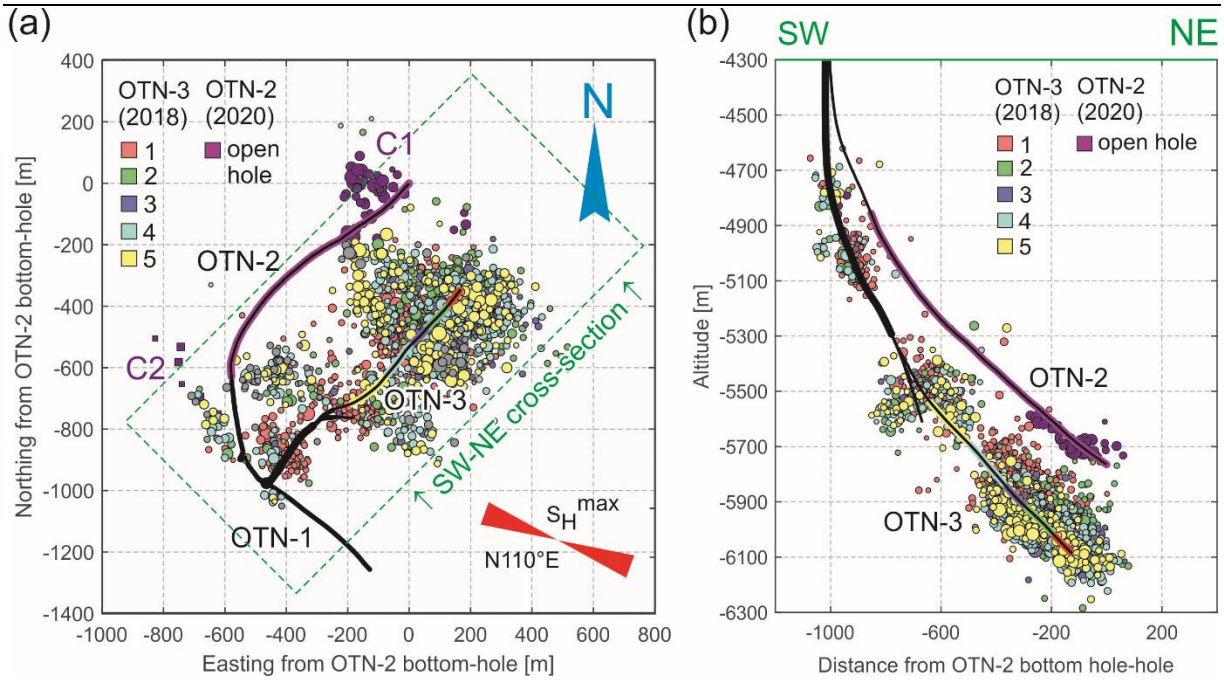

Figure 4. Hypocenters of seismicity from the 2020 stimulation (this study, magenta circles and squares, denoting clusters C1 and C2, respectively) and from past 2018 stimulation (circles color-coded with injection phases 1-5, cf. Leonhardt et al., 2021b). (a): Map view; (b): SW-NE-trending depth section along 45° (SW-NE) azimuth. The colored sections of the OTN-3 and OTN-2 wells indicate isolated stimulation intervals (2018) and the open-hole section (2020), respectively. The size of symbols reflects earthquake magnitudes.

Spatiotemporal evolution of seismic events and focal mechanisms

The spatial distribution of the seismic activity forms two separate clusters C1 (double-difference-relocated events) and C2 (absolute locations) shown in **Figure 4** as magenta circles and squares, respectively. 42 relocated seismic events observed during the stimulation and after shut-in form a cluster close to the bottom end of the OTN-2 well. The epicentral locations of C1 events extends towards NW similar to the seismicity observed in 2018, but the events are located at a ca. 100-200m shallower depth (Fig. 4b). The C2 cluster is formed by 4 earthquakes located in the vicinity of the top part of the open-hole section of the OTN-2 well. These events are situated at similar depths as those observed in the uppermost cluster of the 2018 stimulation (cf. Leonhardt et al., 2021b), reaching further towards the NW. In contrast to 2018 and irrespective of the small relative relocation uncertainties, we did not observe a spatial migration of seismic events during the 2020 injection, which was likely related to the smaller over-pressures applied compared to 2018. The spatial extension of the clusters C1 and C2 suggest fluid migration towards NW/NNW from the open-hole section with no prominent seismicity detected to the SE of the stimulated OTN-2 well.

The quality-constrained double-couple focal mechanisms display oblique strike-slip/thrust reverse faulting events with one nodal plane aligned in NNW-SSE direction (**Figure 5**). The obtained mechanisms are similar to those obtained by Rintamäki et al.(2021) for the two largest events from the same stimulation using FOCMEC software and local and regional polarity data (strike/dip/rake=140°/58°/26°). The focal mechanisms are rotated clockwise by ca. 20° (strike), whereas dip and rake are the same (within the uncertainties obtained by sampling of input data). The observed rotation of focal mechanisms compared to that of Rintamäki et al. (2021) is well-explained by a relatively weak control on the strike and rake of mechanisms due to the limited number of stations at larger epicentral distances. However, the obtained mechanisms are in qualitative agreement with a subset of focal mechanism derived by Leonhardt et al., (2021) using HASH software (Hardebeck and Shearer, 2002) for the seismicity induced by the 2018 stimulation (Family 2, see Fig. 8 in Leonhardt et al. (2021b) for details).

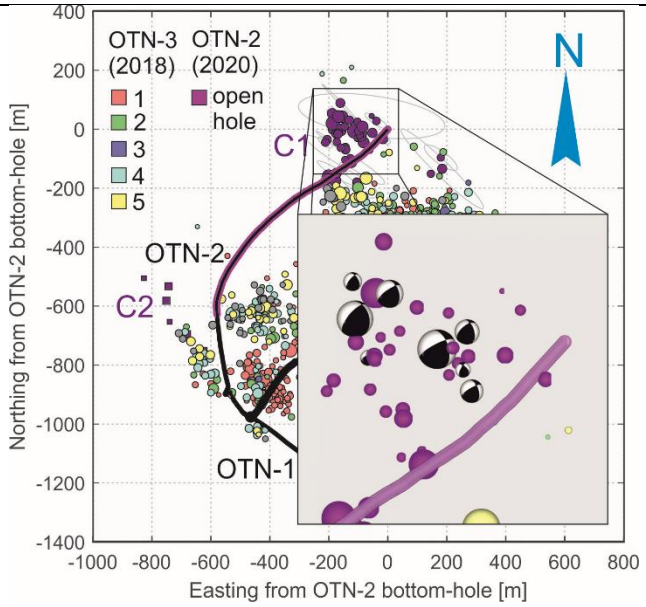

Figure 5. Focal mechanism solutions calculated for the largest earthquakes of the 2020 stimulation using the a double-couple constrained moment tensor inversion. The inset shows orthographic view of focal mechanisms from the direction of earth surface (comparable to the upper-hemisphere projection).

Temporal catalog completeness

Any statistical analysis of seismic *b*-value, inter-event time, inter-event time ratio and magnitude-correlation statistics will depend on the completeness magnitude of the seismic catalog, M_{C}. As in 2018 (cf. Figure 2 in Kwiatek et al., 2019), the 2020 seismic catalog displays strong daily fluctuations of seismic activity related to anthropogenic surface noises. Due to daily anthropogenic noise fluctuations, the earthquake detection threshold roughly follows a sinusoidal pattern increasing by approximately +0.4 and +0.2 during workdays and weekends, respectively (green solid line in Fig. 2a-b). Noise from injection pumps further increased detection level by about +0.3 unit of $M_{\mathrm{L}}^{\mathrm{Hel}}$, masking smaller events (Fig. 2b). For best recording conditions (=no injection and during weekend days), the borehole array

placed in OTN-3 well could detect earthquakes as small as $M_{\mathrm{L}}^{\mathrm{Hel}}$ -1.9 (for signals detected by the borehole array only). Consequently, we found an average magnitude of completeness $M_{\mathrm{C}} = -1.44$ for the seismic catalog covering phases P2-P4 of the 2020 injection (cf. above which the magnitude distribution follows a Gutenberg-Richter power law) (Fig. 3a). However, for the statistical analysis related to triggering statistics we used a more conservative magnitude threshold of $M_{\mathrm{C}}^{*} = -1.25$, which suppressed effects related to short-term catalog incompleteness due to variations in environmental noise levels (Fig. 2b). Using a lower magnitude threshold for the catalog clearly affects the statistical analysis performed in this study (see **Figures S1**, **S2** and **S3** and discussion below for details).

Magnitude correlations

We analyzed the changes in probability $\delta p(\Delta m)$ to observe a magnitude difference $M_{i+1} - M_i < \Delta m$ for events from selected subsets of the earthquake catalog (**Figure 6)** containing only quasi-stable injection periods avoiding the shut-in phases and resting periods while assuming $M_C^{*} = -1.25$. The first selected time period (Fig. 6a) covers the seismicity that occurred during injection phase P1 (from the time when injection rate ramped up to 400 l/s and until ca. 2 hours after the injection shut-in, when the well head pressure dropped below 60 MPa). Here nearly all points of empirical $\delta p(\Delta m)$ fall within 68% confidence lines calculated using multiple resampled distributions of magnitude correlations for which any potential correlations have been destroyed. Moreover, no single point falls outside the 95% confidence interval. This means the selected subset containing phase P1 seismicity does not significantly differ from its randomized version, and thus there is no statistically significant evidence for the existence of event-to-event magnitude correlations in the P1 subset. Accordingly, this also means that short-term local-in-time accelerations or decelerations of seismic energy release are very scarce (if at all present) during injection phase P1. This was also found for magnitude correlations using the entire time period covering phases P2-P4 that include short resting periods in between phases (Fig. 6b) as well as when one considers the individual phases such as P3 alone (Fig. 6c). This is a clear indication of the absence of correlations between magnitudes. Finally, the post-stimulation catalog (Fig. 6d) indicates, as intuitively expected, signatures of weak correlations between magnitudes (where subsequent events of similar magnitude are less likely to occur as expected by random chance) when a more conservative 68% confidence intervals is considered. However, these weak correlations are not significant at the 95% confidence level. Lowering the magnitude of completeness below the conservative threshold of $M_C^{*} = -1.25$ weakens the reliability of inferring magnitude correlations (Fig. S1). Specifically, short-period catalog incompleteness manifests itself in a higher likelihood of subsequent events of similar magnitude. This systematic bias can be clearly seen, e.g., in Fig. S1a-b leading to deviations beyond the 95% confidence level.

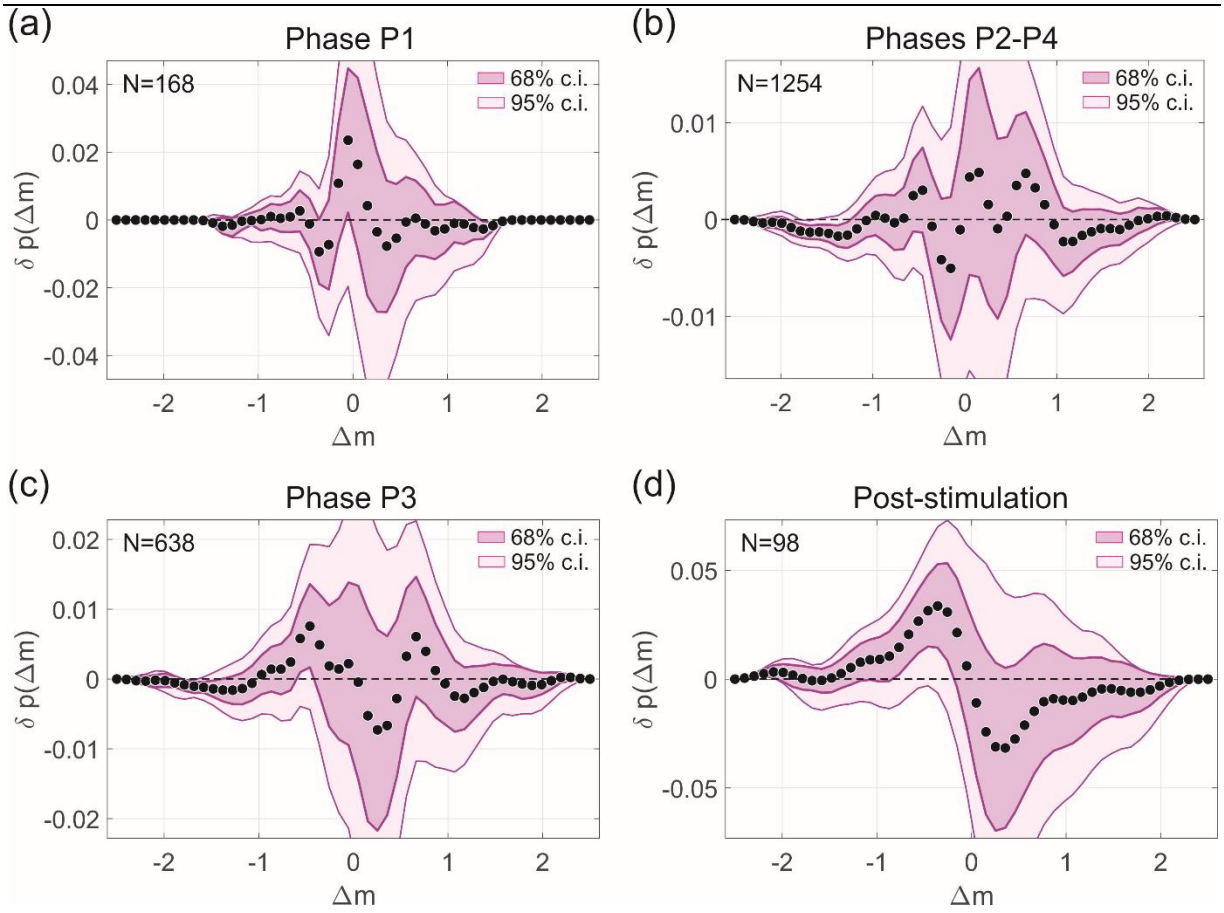

Figure 6. Differences in the probability to observe a magnitude difference $M_{i+1} - M_i < \Delta m$ between selected subset of the catalog containing N earthquakes (black dots) and its randomized versions, which do not exhibit magnitude correlations (eq. 3, light and dark magenta areas correspond to 95% and 68% confidence intervals, respectively). Magnitude correlations correspond to significant deviations from zero. (a): Injection phase P1; (b): Injection phases P2-P4; (c): Injection phase P3; (d): Post-stimulation seismicity (cf. Fig. 2 for time intervals).

Temporal clustering properties

The empirical probability density function of inter-event times, $p(\boldsymbol{\Delta T}/\langle \Delta T \rangle)$ is shown in **Figure 7a** for injection phase P3 containing sufficient number of events above M_C^* thus allowing for reliable estimations. We selected a narrowed time period bounded by dashed lines in Fig. 7b is characterized by a long-lasting and quasi-stable injection without any major interruption but with repeating pressurization episodes (cf. Fig. 2). An empirical distribution (circles in Fig. 7a) was fit to a gamma distribution parameterized by shape and scale coefficients k and B, respectively. We used closed-form estimators of scale and shape parameters that display similar performance as the maximum likelihood estimators (Ye and Chen, 2017). The gamma distribution was previously found to well describe the interevent time distributions in wide range of scales between laboratory experiments and natural earthquakes (see Davidsen and Kwiatek (2013), and references therein). The obtained distribution of inter-event times is practically indistinguishable from the exponential distribution, the probability

distribution of the inter-event times in a Poisson process, where events occur independently at a constant average rate. This strongly suggests that the seismicity follows a Poissonian process.

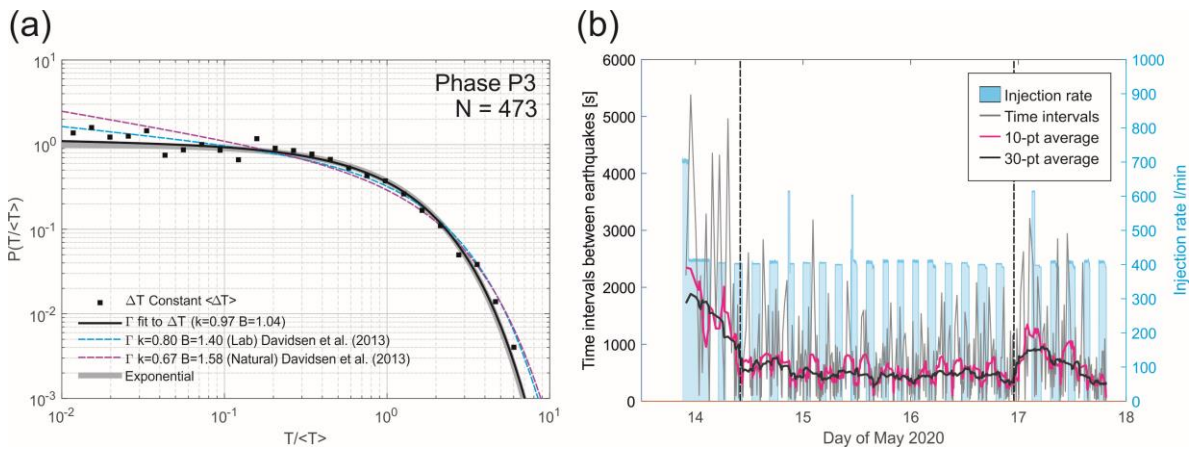

Figure 7. (a): Empirical distribution of interevent times (black squares) and its fit to the gamma distribution (solid black line) for selected time interval of seismicity from phase P3 of injection ($M > M_C^*$). For comparison, gamma fits obtained for laboratory data and induced seismicity (Davidsen and Kwiatek, 2013) and the exponential distribution are shown with dashed cyan, magenta and solid gray lines; (b): Interevent-times of seismic events from phase P3 of injection (gray line) with 10- and 30-points moving average (cyan and black line, respectively). To calculate empirical distribution in (a), the quasi-stable time interval between two dashed vertical lines was used.

This is further confirmed by panels (a-d) of **Figure 8** showing the empirical probability density functions of inter-event time ratios, $p(\boldsymbol{R})$, calculated for selected subsets of the seismic catalog during (Fig. 8a-c) and after stimulation (Fig. 8d). We assumed a conservative magnitude of completeness $M > M_C^*$. It is clearly seen that for the selected catalog, the inter-event time ratios fall within a 95% confidence interval of a (non-homogeneous) Poisson process with the same number of events. This means that these subsets are unlikely to contain any signatures of local-in-time clustering or anti-clustering. Interestingly, this holds for the post-stimulation activity as well (Fig. 8d) where the stress relaxation effects are expected. For comparison, $p(\boldsymbol{R})$ calculated for the aftershock sequence of a M_W 1.9 event recorded in the Mponeng deep gold mine (Kwiatek et al., 2010, 2011) and from the Alpine fault system (cf. Michailos, 2019; Michailos et al., 2019) are shown in Fig. 8e-f. The sequences contain overlapping background seismicity and aftershocks. Theses sequences display clear indications for local temporal clustering of seismicity, as evidenced by strong deviations of empirical $p(\boldsymbol{R})$ which exceed the confidence intervals at the edges. We further constrained the input inter-event time vectors $\boldsymbol{R}$ and

calculated conditional probabilities $p(\boldsymbol{R}|M > -0.8)$ and $p(\boldsymbol{R}|\Delta M < 0)$. The conditioning should emphasize any potential (anti-)clustering behavior because larger events are expected to trigger subsequent events more frequently and also larger events preceding smaller ones promote aftershock sequences that favor triggering. The obtained results suggest the conditioned catalog subsets either do not display significant (antic-)clustering properties (Figs. S2 and S3).

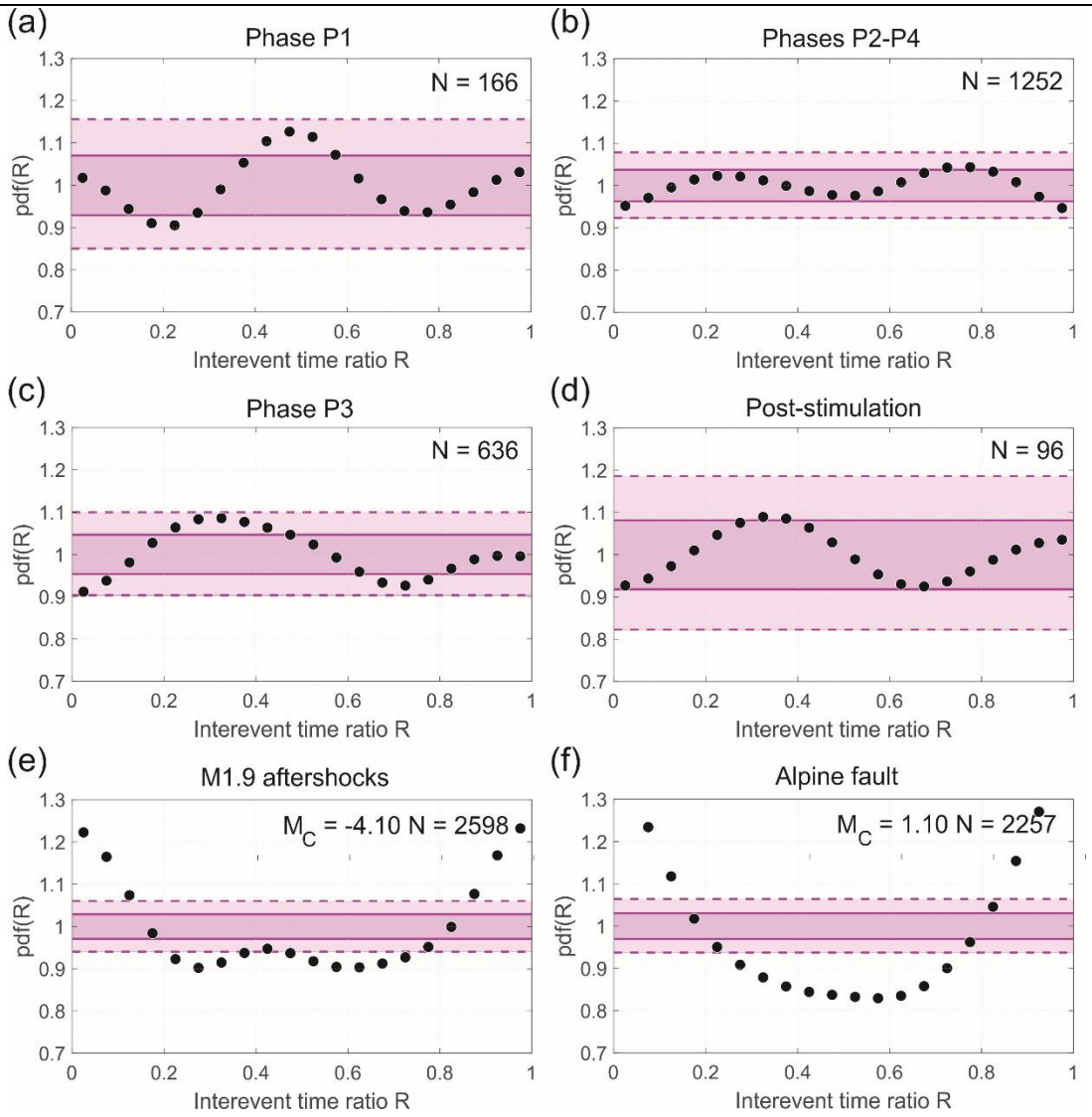

Figure 8. Probability density function of interevent time ratios, $p(\mathbf{R})$, for seismicity from different phases of 2020 stimulation and above the conservative magnitude of completeness, $M_C^* = -1.25$. (a): Phase P1; (b) Phase P2-P4; (c): Phase P3; (d) Post-stimulation. For comparison, (e): Aftershock sequence of $M_W 1.9$ earthquake recorded in Mponeng deep gold mine (Kwiatek et al., 2010, 2011); (f): Alpine fault catalog containing background activity and aftershock sequences (Michailos, 2019; Michailos et al., 2019) are shown (see text for discussion). Solid and dashed magenta lines correspond to 68% and 95% confidence intervals of $p(R)$ expected from events randomly distributed in time, assuming same number of events as in the particular catalog subset.

4 Discussion

The analysis of seismic activity induced by the May 2020 stimulation campaign performed in OTN-2 well within the Helsinki St1 EGS project shows a similar trend as already observed during 2018 OTN-3 well stimulation. Our results confirm a *stable* evolution of induced earthquake activity during a pressure-controlled fluid-injection, with a low potential for the occurrence of unstable/runaway earthquakes. Following Bentz et al. (2020) we define a s*table* evolution of seismicity by low and time-invariant seismic injection efficiency η^{inj} during injection operations, with a maximum magnitude evolution related to injected fluid volume (c.f. Shapiro et al., 2010; McGarr, 2014; van der Elst et al., 2016; Galis et al., 2017). For a *stable* seismicity evolution, the maximum magnitude is bound by the elastic strain energy stored by fluid injection in a geothermal system (Galis et al., 2017). This is in clear contrast to an *unstable* seismicity evolution, where seismic injection efficiency is observed to be either high or continuously increasing such as in the Pohang EGS project (Bentz et al., 2020). We posit that temporal increase in η^{inj} may indicate a pending transition from *stable* conditions with arrestable seismic events to *unstable or run-away* conditions (Galis et al., 2017). Run-away ruptures are driven by tectonic stresses and cannot be controlled by engineering operations. Maximum magnitudes of events are related to the size of faults in the stimulated volume.

Stable, pressure-controlled seismic response to fluid injection in geothermal reservoirs will largely depend on the absence of critically stressed large faults within or near the stimulated rock volume, (McGarr, 2014; Ellsworth et al., 2019). Activation and growth of a small-scale network of randomly distributed fractures and joints may be less prone to host larger seismic events (cf. discussion in Martínez-Garzón et al., 2020). Therefore, near-real-time assessment of spatio-temporal behavior of seismic event locations, focal mechanisms, and temporal evolution of statistical properties such as *b*-value, c-value and d-value (Schoenball et al., 2015; Goebel et al., 2017; Eaton and Igonin, 2018; Dresen et al., 2020) is key to identify the existence/emergence of large fault structures.

In addition to the fault inventory and geometry, the stress state of reservoir faults is important for potential significant stress transfer via earthquake-earthquake interactions (Kwiatek et al., 2019). Fault stress state, static and dynamic stress transfer are known to affect the evolution of seismic activity in a geothermal system (e.g. Schoenball et al., 2012; Martínez-Garzón et al., 2018). There is general consensus that mitigation actions must be applied when stress transfer from earthquakes generates significant stress changes driving seismicity even without fluid injection. However, mitigations may be ineffective to reduce the seismic hazard (Brown and Ge, 2018).

In this study we calculated diagnostic statistical and technological parameters that may ultimately help to characterize the stability of a stimulated geothermal reservoir. In particular, we propose that

533 the stability of (and preferably absence) of earthquake triggering processes is an important
534 characteristic of stable reservoirs. As shown in this study, information on earthquake interactions
535 and triggering can be achieved in near-real-time using simple statistical characteristics of the seismic
536 catalog.

537 The seismicity induced by stimulation campaigns in the Helsinki geothermal project are well-
538 constrained examples of stable induced seismicity passively responding to injection operations. Both
539 stimulation campaigns share common features including comparable and generally time-invariant
540 seismic injection efficiencies and *b*-values (Fig. 3a-b). Following Main (1991), stationary *b*-values
541 indicate a stable damage evolution, i.e. lack of progressive coalescence of fractures towards system-
542 wide failure. For both stimulations no notable time delays existed between start of pumping and
543 seismicity during the entire stimulation. Seismicity occurred in spatially-broad zones once ca. 70 MPa
544 well-head pressure was exceeded. Since no Kaiser effect (Kaiser, 1953; Baisch et al., 2002) was
545 observed, these observations suggest that a distributed network of fractures was re-activated beyond
546 a critical well-head pressure during stimulation. The observed invariance of *b*-values may also indicate
547 limited overall stress buildup in the reservoir (Scholz, 1968; Schorlemmer et al., 2005), likely due to
548 injection-induced stresses being distributed in a 3D-volume of distributed fractures rather than on a
549 single major structure. Observations of *b*-values are in contrast to data from Basel, Switzerland or
550 Pohang, South Korea (Bachmann et al., 2012; Ellsworth et al., 2019) where decreasing *b*-values were
551 observed towards the occurrence of larger run-away earthquakes on a major fault.

552 Evolution of maximum event magnitudes during the 2020 and 2018 stimulations follows a trend
553 predicted by Galis et al. (2017) or van der Elst et al. (2016) for pressure-controlled seismicity. Following
554 the former study, the observed trend suggests that the maximum event magnitude is related to the
555 amount of elastic energy stored in the reservoir due to fluid injection. Lab experiments and field
556 observations suggest that energy dissipation involves significant contribution from aseismic (here
557 interpreted as out-of-the-seismic band, cf. Dresen et al., 2020) deformation (McGarr and Barbour,
558 2018). However, the existing models relating seismic moment evolution and maximum magnitude of
559 events to the injected total fluid volume do not capture the effect of injection rate on seismicity and
560 aseismic deformation. Flow rate and the rate of pore fluid pressure build-up are expected to affect
561 induced seismic activity, as was observed from waste water injection (Weingarten et al., 2015),
562 laboratory tests (Passelègue et al., 2018; Wang et al., 2020b) and numerical modeling (Almakari et al.,
563 2019; Rudnicki and Zhan, 2020). This highlights the importance of hydraulic energy input rate as the
564 actual parameter controlling maximum magnitude and seismic hazard during stable phases of injection
565 operations. For time invariant *b*-values, seismic hazard is related solely to seismicity rate changes.
566 Wang et al. (2020b) showed that that the mechanical response (slip rate / moment rate) of a single

planar fault, as well as the associated small-scale acoustic emission activity (moment rate) may vary significantly with respect to pressurization rate (~hydraulic energy rate). With increasing pore fluid pressurization rate, seismic moment release changed from stable and almost linear behavior to short "run-away" slip at high pressurizations rates. During the 2020 Helsinki OTN-2 well stimulation, we did not observe a non-linear increase of seismic energy release in response to hydraulic energy input. This was evidenced by a stable seismic injection efficiency, likely favored by very low injection pressures applied. Only during a relatively short period when high hydraulic energy input rates were applied during the 2018 Helsinki OTN-3 well stimulation, we observed a clear acceleration of seismic energy release leading to progressive increase of seismic injection efficiency (cf. Kwiatek et al., 2019 for details). However, with immediate mitigation procedures applied in response to the occurrence of large magnitude events (Ader et al., 2019), seismic injection efficiency could be stabilized again. In summary, both stimulation campaigns in 2018 and 2020 represent pressure-controlled, stable induced seismicity where seismic/aseismic energy dissipation is clearly related to hydraulic energy input, with limited possibility for runaway ruptures to occur.

In many geothermal systems induced seismicity continues beyond shut-in. At the Basel Deep Heat Mining HDR site seismicity following the stimulation campaign in 2006 is still ongoing after 15 years. In Helsinki, the occurrence of a relatively large earthquake of magnitude $M_{\mathrm{L}}^{\mathrm{Hel}} = 1.2$ in April 2020 before the 2020 stimulation campaign in OTN-2 was unexpected. Within the framework described in previous paragraph, the occurrence of this event, as well as the associated seismicity in preceding months could be related to the relaxation of the elastic strain energy accumulated in the reservoir during the 2018 stimulation. However, some natural earthquakes ($M_{\mathrm{W}}1.7$ and $M_{\mathrm{W}}1.4$, see Kwiatek et al., 2019 for details) did occur at epicentral distances not exceeding a few km from the project site in 2011. Thus it is difficult to attribute any event within this time period to being natural or triggered/induced without detailed information on engineering operations performed at the site.

For the 2018 and 2020 stimulation campaigns, we found seismic activity to quickly decline within 24h following each shut-in (Fig. 2a, d). This supports our contention that the observed seismicity during the stimulations was entirely due to a local stress perturbation induced by injection. Interestingly, we found that the cumulative seismic energy release within 12 hours after phases P1-P4 of the 2020 injection scales with the total hydraulic energy accumulated during the injection phase (**Figure 9a**). Also, the rate of seismic moment decrease during shut-in phases is similar for most post-shut-in periods, and roughly scales as $\sum M_0(t) \propto t^{\alpha}$, where t is the time since the begin of shut-in (Fig. 9b) and α slightly above the unity. The decrease of seismic moment is comparable to a decrease in seismic activity as expressed by the Omori law (Utsu, 1961). However, the rate decay occurs without associated

temporal changes in the *b*-value that are sometimes reported for aftershock sequences (e.g. Gulia and Wiemer, 2019).

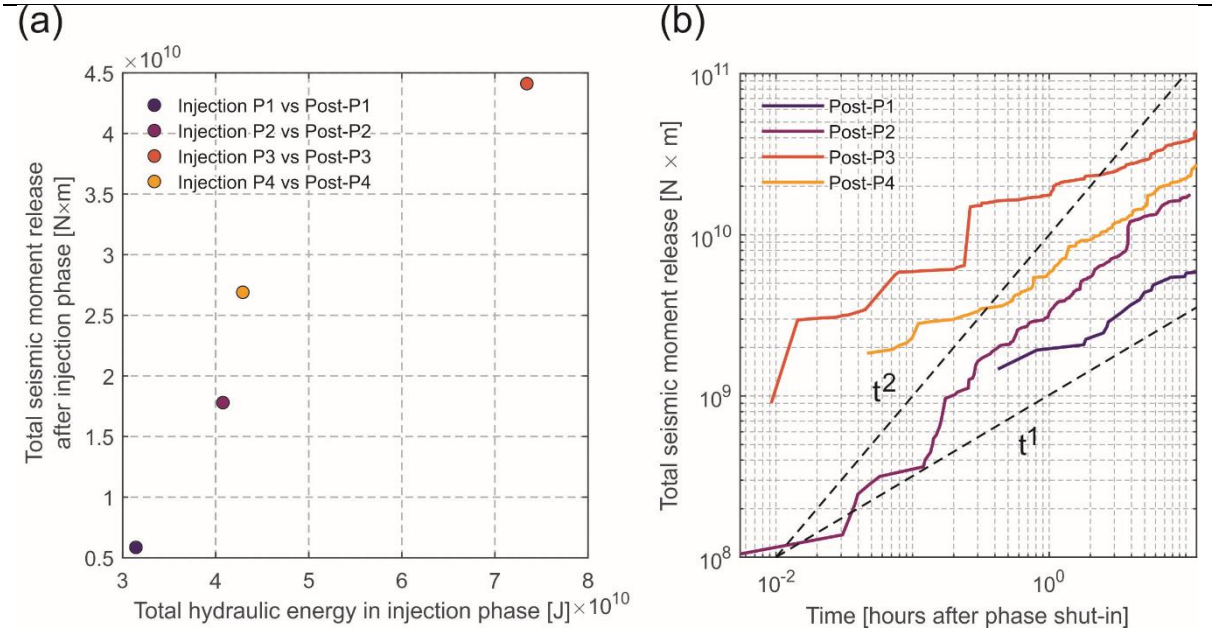

Figure 9. (a) Relation between total hydraulic energy of injection phase P1-P4 and total seismic moment releases within 12-hour time period following the injection phase. (b) Seismic moment release evolution within 12 hours following injection phases P1-P4.

The observed seismic response clearly relates to the reservoir structure. There is no evidence for activation of a larger fault that was previously unknown within the reservoir or its immediate surrounding. Relocated events (location error ±41 m in horizontal direction) of cluster C1 (Fig. 4) suggest extension of a broad damage zone already observed during 2018 OTN-3 stimulation further to the NW. Focal mechanisms calculated using moment tensor inversion display one nodal plane in good agreement with the regional stress field (cf. Leonhardt et al., 2021), suggesting that the stimulation reactivated a spatially-broad network of fractures trending mostly NW-NNW, but at shallower depth than observed in 2018 (cf. Fig. 5).

Kwiatek et al. (2019) found that > 85% of seismic events induced by the 2018 stimulation displayed properties of background seismicity. The events followed a quasi-stationary Poissonian process with earthquakes randomly distributed over the stimulated volume and in time. A spatio-temporal analysis could not be performed for the 2020 seismicity catalog due to a limited number of seismic events. Instead, we employed a number of simple statistical measures of clustering in the time domain, all confirming very limited interaction between earthquakes from the 2020 seismic catalog. The empirical distribution of inter-event times $p(\boldsymbol{\Delta T}/\langle \Delta T \rangle)$ of seismicity from Phase P3 of the injection campaign

conform to an exponential distribution (Gamma distribution fit parameters: k=0.98, B=1.04). This indicates that earthquakes occur randomly in time, when we properly select the catalog accounting for changing seismicity rates due to variation in the injection rates and for temporal variabilities of M_C. Indeed, the statistical analysis of inter-event time ratios revealed no temporal clustering and anticlustering between earthquakes occurring during and after the stimulation campaign (Fig. 8a-d). The empirical distributions were statistically indistinguishable from (non-homogeneous) Poissonian-distributed seismicity as clearly shown for isolated injection phases P1 and P3 (Fig. 8a, c). Even the subset of the catalog covering phases P2-P4 (Fig. 8b) that includes resting periods, as well as the post-injection catalog (Fig. 8d) do not show any signatures of temporal (anti-)clustering. This is also the case when we further condition the catalog subsets trying to emphasize the potential (anti-)clustering behaviors (Fig. S2-S3). We therefore conclude that earthquakes forming the catalog occur randomly in time following a (non-homogeneous) Poissonian process. The variations in seismicity rate are modulated by the hydraulic energy input rate, as expected for induced seismicity (Langenbruch et al., 2011; Goebel et al., 2019), but show no temporal clustering – in contrast to other fluid-driven settings (Maghsoudi et al., 2018; Karimi and Davidsen, 2021). Neither the enhanced stressing rates due to fluid injection nor stress relaxation after the stimulation phases, nor the localization of seismicity within confined zones caused triggering.

Frequently, a prominent structure such as a fault, which causes local stress concentration, results in earthquake triggering (Davidsen et al., 2017, 2021). However, no major fault was reported for the stimulated reservoir, which may explain the lack of triggering in agreement with Schoenball et al. (2012) for Soultz-sous-Forets/France geothermal site and Martínez-Garzón et al. (2018) for The Geysers geothermal field in California. Last, we note the sensitivity of $p(\boldsymbol{\Delta T}/\langle \Delta T \rangle)$ distribution to the choice of M_C and abrupt injection rate changes that needed to be accounted for by careful selection of the subsets. Ignoring these problems led to gamma-type distributions (e.g. Davidsen and Kwiatek, 2013). Therefore, detecting very fine details of interevent time statistics must be always associated with high-quality seismic monitoring and careful assessment of catalog completeness.

Magnitude correlations are insignificant for 95% confidence intervals in all analyzed cases. These include subsets of the catalog covering selected stimulation phases (Fig. 6a-c) and the post-stimulation catalog (Fig. 6d). Probability differences $\delta p(\Delta m)$ do not deviate significantly from zero considering confidence intervals. This indicates a lack of local-in-time accelerations or decelerations of seismic energy release in the catalog, in agreement to studies of induced nano- and picoseismicity (Davidsen et al., 2012). The observed lack of magnitude correlations supports the assumption of independent earthquake magnitudes and applying probabilistic methods of seismic hazard assessment for the stimulation site (Ader et al., 2019). The lack of statistically significant magnitude correlations also

argues against existence of any cascade-type nucleation processes (e.g. Ellsworth and Beroza, 1995; McLaskey, 2019). Cascade processes rests on some form of stress transfer between earthquakes, for which we find no statistical evidence down to our conservative magnitude of completeness of $M_C^* = -1.25$, i.e. faults/fracture sizes of the order of a few meters. Similar to what has been found for previous statistical properties, magnitude correlations are also sensitive to variations in completeness level caused by injection- and day/night cycle-related changes in earthquakes detectability.

5 Conclusions

Two hydraulic stimulation campaigns performed in 2018 and 2020 in two different wells in the Helsinki suburban area as part of the St1 Deep Heat project each resulted a stable evolution of induced seismic activity that could be controlled by adjusting the injection operations. We posit that the pressure-controlled seismicity evolved in response to an adaptive injection strategy balancing the hydraulic energy input with seismic energy release output and favored by reservoir structures and stress state. In an effort to identify proxies characterizing seismicity evolution as either stable or run-away we analyzed a series of seismic parameters signifying potential interaction between the earthquakes. We found that the absence of earthquake – earthquake triggering is an important indicator for a stable injection. Using the proposed simple diagnostic measures of interactions in near-real-time monitoring may allow to detect potential deviations from a stable state, potentially indicating increasing seismic hazard. We summarize the characteristics of stable reservoir as observed in the 2018 and 2020 stimulations as follows:

1) The seismicity down to at least magnitude -1.25 (source sizes of a couple of m) passively responded to injection operations. It displays representative properties of background seismicity that can be well described by a non-stationary Poisson process and is modulated by the hydraulic energy input rate. Although the seismicity tends to cluster in space and time in response to fluid injection, no interaction between earthquakes is observed despite highly varying hydraulic energy input rates.

2) Seismic energy output rate, without significant temporal variations in b-value indicating activation of a stationary and spatialy-distributed fracture network, is proportional to the hydraulic energy input rate. The ratio of seismic to hydraulic energy is not changing over time substantially.

3) The maximum magnitude in both 2018 and 2020 stimulations is bound by the current level of elastic strain energy stored in the geothermal system due to injection, through total hydraulic energy input and input rate.

4) The relocated seismic data, their relative precision in comparison to total spatial extent of the seismicity clearly suggest (re)activation of the volume of distributed and likely subparallel fractures.

The limited magnitudes of seismic events and low event density in the stimulated reservoir volume inhibit triggering. Instead, fluid injection caused largely aseismic deformation, i.e. brittle processes not capture by the seismic band of the monitoring system.

5) The response of the induced reservoir seismicity to the injection operations supports the use of deterministic models and classical probabilistic methodologies for seismic hazard assessment at this geothermal project.

Acknowledgements

We would like to thank M. Uski, T. Vuorinen, K. Oinonen, J. Kortstrom, B. Orlecka-Sikora, and S. Lasocki for useful discussions during preparation of the manuscript. P.M.G. acknowledges funding from the Helmholtz Association in the frame of the Young Investigators Group VH-NG-1232 (SAIDAN).

Data

Catalog of detections, located and relocated events and focal mechanisms is available as separate data publication:

Kwiatek, Grzegorz; Martínez-Garzón, Patricia; Karjalainen, Aino (2026): Earthquake catalog of induced seismicity associated with 2020 hydraulic stimulation campaign at OTN-2 well in Helsinki, Finland. GFZ Data Services, DOI: 10.5880/GFZ.4.2.2022.001.

References

Ader, T. et al. (2019). Design and implementation of a traffic light system for deep geothermal well stimulation in Finland, *J. Seismol.* doi 10.1007/S3950-019-09853-y. [online] Available from: https://doi.org/10.1007/S3950-019-09853-y

Alghannam, M., and R. Juanes (2020). Understanding rate effects in injection-induced earthquakes, *Nat. Commun.* **11**, no. 1, 3053, doi 10.1038/s41467-020-16860-y.

Almakari, M., P. Dublanchet, H. Chauris, and F. Pellet (2019). Effect of the Injection Scenario on the Rate and Magnitude Content of Injection-Induced Seismicity: Case of a Heterogeneous Fault, *J. Geophys. Res. Solid Earth* **124**, no. 8, 8426–8448, doi 10.1029/2019JB017898.

Amemoutou, A., P. Martínez-Garzón, G. Kwiatek, J. L. Rubinstein, and M. Bohnhoff (2021). Earthquake Source Mechanisms and Stress Field Variations Associated With Wastewater-Induced Seismicity in Southern Kansas, USA, *J. Geophys. Res. Solid Earth* **126**, no. 7, e2020JB021625, doi 10.1029/2020JB021625.

Bachmann, C. E., S. Wiemer, B. P. Goertz-Allmann, and J. Woessner (2012). Influence of pore-pressure on the event-size distribution of induced earthquakes, *Geophys. Res. Lett.* **39**, no. 9, doi 10.1029/2012GL051480. [online] Available from: https://doi.org/10.1029/2012GL051480 (Accessed 5 September 2018)

Baisch, S. (2020). Inferring In Situ Hydraulic Pressure From Induced Seismicity Observations: An Application to the Cooper Basin (Australia) Geothermal Reservoir, *J. Geophys. Res. Solid Earth* **125**, no. 8, e2019JB019070.

Baisch, S., M. Bohnhoff, L. Ceranna, Y. Tu, and H.-P. Harjes (2002). Probing the crust to 9-km depth: Fluid injection experiments and induced seismicity at the KTB superdeep drilling hole, Germany, *Bull Seism. Soc Am* **92**, no. 6, 2369–2380.

Bentz, S., P. Martínez-Garzón, G. Kwiatek, M. Bohnhoff, and J. Renner (2018). Sensitivity of Full Moment Tensors to Data Preprocessing and Inversion Parameters: A Case Study from the Salton Sea Geothermal Field, *Bull. Seismol. Soc. Am.* **108**, no. 2, 588–603, doi 10.1785/0120170203.

Bentz, S., G. Kwiatek, P. Martínez-Garzón, M. Bohnhoff, and G. Dresen (2020). Seismic moment evolution during hydraulic stimulations, *Geophys. Res. Lett.* **47**, e2019GL086185, doi 10.1029/2019GL086185.

Brown, M. R. M., and S. Ge (2018). Small Earthquakes Matter in Injection-Induced Seismicity, *Geophys. Res. Lett.* **45**, no. 11, 5445–5453.

Catalli, F., M.-A. Meier, and S. Wiemer (2013). The role of Coulomb stress changes for injection-induced seismicity: The Basel enhanced geothermal system, *Geophys. Res. Lett.* **40**, no. 1, 72–77, doi 10.1029/2012GL054147.

Catalli, F., A. P. Rinaldi, V. Gischig, M. Nespoli, and S. Wiemer (2016). The importance of earthquake interactions for injection-induced seismicity: Retrospective modeling of the Basel Enhanced Geothermal System, *Geophys. Res. Lett.* **43**, no. 10, 4992–4999, doi 10.1002/2016GL068932.

Cesca, S., A. Rohr, and T. Dahm (2013). Discrimination of induced seismicity by full moment tensor inversion and decomposition, *J. Seismol.* **17**, no. 1, 147–163, doi 10.1007/S3950-012-9305-8.

Cochran, E. S., A. Wickham-Piotrowski, K. B. Kemna, R. M. Harrington, S. L. Dougherty, and A. F. Peña Castro (2020). Minimal Clustering of Injection-Induced Earthquakes Observed with a Large-n Seismic Array, Bulletin of the Seismological Society of America 110, no. 5, 2005–2017, doi 10.1785/0120200101.

743 Davi, R., V. Vavryčuk, E.-M. Charalampidou, and G. Kwiatek (2013). Network sensor calibration for
744 retrieving accurate moment tensors of acoustic emissions, *Int. J. Rock Mech. Min. Sci.* **62**, no. 0, 59–
745 67, doi 10.1016/j.ijrmms.2013.04.004.

746 Davidsen, J., and G. Kwiatek (2013). Earthquake interevent time distribution for induced micro-,
747 nano- and picoseismicity, *Phys. Rev. Lett.* **110**, 068501, doi 10.1103/PhysRevLett.110.068501.

748 Davidsen, J., G. Kwiatek, and G. Dresen (2012). No Evidence of Magnitude Clustering in an Aftershock
749 Sequence of Nano- and Picoseismicity, *Phys. Rev. Lett.* **108**, 038501, doi
750 10.1103/PhysRevLett.108.038501.

751 Davidsen, J., G. Kwiatek, E.-M. Charalampidou, T. H. W. Goebel, S. Stanchits, M. Rueck, and G. Dresen
752 (2017). Triggering processes in rock fracture, *Phys. Rev. Lett.* **119**, 068501, doi
753 10.1103/PhysRevLett.119.068501.

754 Davidsen, J., T. Goebel, G. Kwiatek, S. Stanchits, J. Baró, and G. Dresen (2021). What Controls the
755 Presence and Characteristics of Aftershocks in Rock Fracture in the Lab?, *J. Geophys. Res. Solid Earth*
756 **126**, no. 10, e2021JB022539, doi 10.1029/2021JB022539.

757 Dresen, G., G. Kwiatek, T. Goebel, and Y. Ben-Zion (2020). Seismic and Aseismic Preparatory
758 Processes Before Large Stick–Slip Failure, *Pure Appl. Geophys.* doi 10.1007/s00024-020-02605-x.
759 [online] Available from: https://doi.org/10.1007/s00024-020-02605-x

760 Eaton, D. W., and N. Igonin (2018). What controls the maximum magnitude of injection-induced
761 earthquakes?, *Lead. Edge* **37**, no. 2, 135–140, doi 10.1190/tle37020135.1.

762 Ellsworth, W. L., and G. C. Beroza (1995). Seismic Evidence for an Earthquake Nucleation Phase,
763 *Science* **268**, no. 5212, 851–855, doi 10.1126/science.268.5212.851.

764 Ellsworth, W. L., D. Giardini, J. Townend, S. Ge, and T. Shimamoto (2019). Triggering of the Pohang,
765 Korea, Earthquake (Mw 5.5) by Enhanced Geothermal System Stimulation, *Seismol. Res. Lett.* **90**, no.
766 5, 1844–1858, doi 10.1785/0220190102.

767 Elst, N. J. van der, and E. E. Brodsky (2010). Connecting near-field and far-field earthquake triggering
768 to dynamic strain, *J. Geophys. Res. Solid Earth* **115**, no. B7. [online] Available from:
769 https://onlinelibrary.wiley.com/doi/abs/10.1029/2009JB006681 (Accessed 8 February 2022)

770 van der Elst, N. J., M. T. Page, D. A. Weiser, T. H. W. Goebel, and S. M. Hosseini (2016). Induced
771 earthquake magnitudes are as large as (statistically) expected, *J. Geophys. Res. Solid Earth* **121**, no. 6,
772 4575–4590, doi 10.1002/2016JB012818.

Font, Y., H. Kao, S. Lallemand, C.-S. Liu, and L.-Y. Chiao (2004). Hypocentre determination offshore of eastern Taiwan using the Maximum Intersection method, *Geophys. J. Int.* **158**, no. 2, 655–675, doi 10.1111/j.1365-246X.2004.02317.x.

Galis, M., J. P. Ampuero, P. M. Mai, and F. Cappa (2017). Induced seismicity provides insight into why earthquake ruptures stop, *Sci. Adv.* **3**, no. 12, doi 10.1126/sciadv.aap7528. [online] Available from: http://advances.sciencemag.org/content/3/12/eaap7528.abstract

Gischig, V. S., and S. Wiemer (2013). A stochastic model for induced seismicity based on non-linear pressure diffusion and irreversible permeability enhancement, *Geophys. J. Int.* **194**, no. 2, 1229–1249, doi 10.1093/gji/ggt164.

Goebel, T. H. W., G. Kwiatek, T. W. Becker, E. E. Brodsky, and G. Dresen (2017). What allows seismic events to grow big?: Insights from b-value and fault roughness analysis in laboratory stick-slip experiments, *Geology* **45**, no. 9, 815–818, doi 10.1130/G39147.1.

Goebel, T. H. W., Z. Rosson, E. E. Brodsky, and J. I. Walter (2019). Aftershock deficiency of induced earthquake sequences during rapid mitigation efforts in Oklahoma, *Earth Planet. Sci. Lett.* **522**, 135–143, doi 10.1016/j.epsl.2019.06.036.

Gulia, L., and S. Wiemer (2019). Real-time discrimination of earthquake foreshocks and aftershocks, *Nature* **574**, no. 7777, 193–199, doi 10.1038/s41586-019-1606-4.

Hanks, T. C., and H. Kanamori (1979). A moment magnitude scale, *J Geophys Res* **84**, 2348–2350.

Hardebeck, J. L., and P. M. Shearer (2002). A New Method for Determining First-Motion Focal Mechanisms, *Bull. Seismol. Soc. Am.* **92**, no. 6, 2264, doi 10.1785/0120010200.

Hastings, W. K. (1970). Monte Carlo Sampling Methods Using Markov Chains and Their Applications, *Biometrica* **57**, no. 1, 97–109.

Hillers, G., T. A. T. Vuorinen, M. R. Uski, J. T. Kortström, P. B. Mäntyniemi, T. Tiira, P. E. Malin, and T. Saarno (2020). The 2018 Geothermal Reservoir Stimulation in Espoo/Helsinki, Southern Finland: Seismic Network Anatomy and Data Features, *Seismol. Res. Lett.* **91**, no. 2A, 770–786, doi 10.1785/0220190253.

Kagan, Y. Y. (2007). Simplified algorithms for calculating double-couple rotation, *Geophys. J. Int.* **171**, no. 1, 411–418.

Kaiser, J. (1953). Kenntnisse und Folgerungen aus der Messung von Geräuschen bei Zugbeanspruchung von metallischen Werkstoffen, *Arch. Für Isenhütten-Wesen* **24**, 43–45, doi 10.1002/srin.195301381.

Karimi, K., and J. Davidsen (2021). Aftershock Triggering and Spatial Aftershock Zones in Fluid-Driven Settings: Discriminating Induced Seismicity From Natural Swarms, *Geophys. Res. Lett.* **48**, no. 15, e2020GL092267, doi 10.1029/2020GL092267.

Kroll, K. A., and E. S. Cochran (2021). Stress Controls Rupture Extent and Maximum Magnitude of Induced Earthquakes, Geophysical Research Letters 48, no. 11, e2020GL092148, doi 10.1029/2020GL092148.

Kwiatek, G., K. Plenkers, M. Nakatani, Y. Yabe, G. Dresen, and J. Group (2010). Frequency-Magnitude Characteristics Down to Magnitude -4.4 for Induced Seismicity Recorded at Mponeng Gold Mine, South Africa, *Bull. Seismol. Soc. Am.* **100**, no. 3, 1167–1173, doi 10.1785/0120090277.

Kwiatek, G., K. Plenkers, and G. Dresen (2011). Source Parameters of Picoseismicity Recorded at Mponeng Deep Gold Mine, South Africa: Implications for Scaling Relations, *Bull. Seismol. Soc. Am.* **101**, no. 6, 2592–2608, doi 10.1785/0120110094.

Kwiatek, G., P. Martínez-Garzón, G. Dresen, M. Bohnhoff, H. Sone, and C. Hartline (2015). Effects of long-term fluid injection on induced seismicity parameters and maximum magnitude in northwestern part of The Geysers geothermal field, *J. Geophys. Res. Solid Earth* **120**, doi 10.1002/2015JB012362.

Kwiatek, G., P. Martínez-Garzón, and M. Bohnhoff (2016). HybridMT: A MATLAB/Shell Environment Package for Seismic Moment Tensor Inversion and Refinement, *Seismol. Res. Lett.* **87**, no. 4, 964–976, doi 10.1785/0220150251.

Kwiatek, G. et al. (2019). Controlling fluid-induced seismicity during a 6.1-km-deep geothermal stimulation in Finland, *Sci. Adv.* **5**, no. 5, eaav7224, doi 10.1126/sciadv.aav7224.

Langenbruch, C., C. Dinske, and S. A. Shapiro (2011). Inter event times of fluid induced earthquakes suggest their Poisson nature, *Geophys. Res. Lett.* **38**, no. 21. [online] Available from: https://onlinelibrary.wiley.com/doi/abs/10.1029/2011GL049474 (Accessed 7 February 2022)

Lasocki, S., and E. E. Papadimitriou (2006). Magnitude distribution complexity revealed in seismicity from Greece, *J. Geophys. Res. Solid Earth* **111**, no. B11, doi 10.1029/2005JB003794. [online] Available from: https://doi.org/10.1029/2005JB003794 (Accessed 28 August 2018)

Leonhardt, M., G. Kwiatek, P. Martinez-Garzon, and P. Heikkinen (2021a). Earthquake catalog of induced seismicity recorded during and after stimulation of Enhanced Geothermal System in Helsinki,

832 Finland, *GFZ Data Serv.* doi 10.5880/GFZ.4.2.2021.001. [online] Available from:
833 https://doi.org/10.5880/GFZ.4.2.2021.001

834 Leonhardt, M., G. Kwiatek, P. Martínez-Garzón, M. Bohnhoff, T. Saarno, P. Heikkinen, and G. Dresen
835 (2021b). Seismicity during and after stimulation of a 6.1 km deep enhanced geothermal system in
836 Helsinki, Finland, *Solid Earth* **12**, no. 3, 581–594, doi 10.5194/se-12-581-2021.

837 Lord-May, C., J. Baró, D. W. Eaton, and J. Davidsen (2020). Seismic hazard due to fluid injections,
838 *Phys. Rev. Res.* **2**, no. 4, 043324, doi 10.1103/PhysRevResearch.2.043324.

839 Maghsoudi, S., D. W. Eaton, and J. Davidsen (2016). Nontrivial clustering of microseismicity induced
840 by hydraulic fracturing, *Geophys. Res. Lett.* **43**, no. 20, 10,672-10,679, doi 10.1002/2016GL070983.

841 Maghsoudi, S., J. Baró, A. Kent, D. Eaton, and J. Davidsen (2018). Interevent Triggering in
842 Microseismicity Induced by Hydraulic Fracturing, *Bull. Seismol. Soc. Am.* **108**, no. 3A, 1133–1146, doi
843 10.1785/0120170368.

844 Main, I. G. (1991). A modified Griffith criterion for the evolution of damage with a fractal distribution
845 of crack lengths: application to seismic event rates and b-values, *Geophys. J. Int.* **107**, no. 2, 353–362,
846 doi 10.1111/j.1365-246X.1991.tb00830.x.

847 Martínez-Garzón, P., G. Kwiatek, M. Bohnhoff, and G. Dresen (2017). Volumetric components in the
848 earthquake source related to fluid injection and stress state, *Geophys. Res. Lett.* **44**, no. 2, 800–809,
849 doi 10.1002/2016GL071963.

850 Martínez-Garzón, P., I. Zaliapin, Y. Ben-Zion, G. Kwiatek, and M. Bohnhoff (2018). Comparative Study
851 of Earthquake Clustering in Relation to Hydraulic Activities at Geothermal Fields in California, *J.*
852 *Geophys. Res. Solid Earth* **123**, no. 5, 4041–4062, doi 10.1029/2017JB014972.

853 Martínez-Garzón, P., G. Kwiatek, S. Bentz, M. Bohnhoff, and G. Dresen (2020). Induced earthquake
854 potential in geothermal reservoirs: Insights from The Geysers, California, *Lead. Edge* **39**, no. 12, 873–
855 882, doi 10.1190/tle39120873.1.

856 Maxwell, S. C. (2011). What does microseismic tell us about hydraulic fracture deformation, *CSEG*
857 *Rec. - Focus Artic.* **36**, no. 8.

858 McGarr, A. (2014). Maximum magnitude earthquakes induced by fluid injection, *J. Geophys. Res.*
859 *Solid Earth* **119**, no. 2, 1008–1019, doi 10.1002/2013JB010597.

860 McGarr, A., and A. J. Barbour (2018). Injection-Induced Moment Release Can Also Be Aseismic,
861 *Geophys. Res. Lett.* **45**, no. 11, 5344–5351, doi 10.1029/2018GL078422.

McLaskey, G. C. (2019). Earthquake Initiation From Laboratory Observations and Implications for Foreshocks, *J. Geophys. Res. Solid Earth* **124**, no. 12, 12882–12904.

Meredith, P. G., and B. K. Atkinson (1983). Stress corrosion and acoustic emission during tensile crack propagation in Whin Sill dolerite and other basic rocks, *Geophys. J. Int.* **75**, no. 1, 1–21, doi 10.1111/j.1365-246X.1983.tb01911.x.

Metropolis, N., A. Rosenbluth, M. Rosenbluth, A. Teller, and E. Teller (1953). Equation of state calculations by fast computing machines, *J Chem Phys* **21**, 1087–1092, doi 10.1063/1.1699114.

Michailos, K. (2019). Southern Alps, New Zealand microseismicity earthquake catalog, [online] Available from: https://doi.org/10.5281/zenodo.3529755

Michailos, K., E. G. C. Smith, C. J. Chamberlain, M. K. Savage, and J. Townend (2019). Variations in Seismogenic Thickness Along the Central Alpine Fault, New Zealand, Revealed by a Decade's Relocated Microseismicity, *Geochem. Geophys. Geosystems* **20**, no. 1, 470–486.

Passelègue, François. X., N. Brantut, and T. M. Mitchell (2018). Fault Reactivation by Fluid Injection: Controls From Stress State and Injection Rate, *Geophys. Res. Lett.* **45**, no. 23, 12,837-12,846, doi 10.1029/2018GL080470.

Rintamäki, A. E. et al. (2021). A Seismic Network to Monitor the 2020 EGS Stimulation in the Espoo/Helsinki Area, Southern Finland, *Seismol. Res. Lett.* doi 10.1785/0220210195. [online] Available from: https://doi.org/10.1785/0220210195 (Accessed 7 February 2022)

Rudnicki, J. W., and Y. Zhan (2020). Effect of Pressure Rate on Rate and State Frictional Slip, *Geophys. Res. Lett.* **47**, no. 21, e2020GL089426, doi 10.1029/2020GL089426.

Schoenball, M., C. Baujard, T. Kohl, and L. Dorbath (2012). The role of triggering by static stress transfer during geothermal reservoir stimulation, *J. Geophys. Res. Solid Earth* **117**, no. B9, doi 10.1029/2012JB009304. [online] Available from: https://doi.org/10.1029/2012JB009304 (Accessed 7 February 2022)

Schoenball, M., N. C. Davatzes, and J. M. G. Glen (2015). Differentiating induced and natural seismicity using space-time-magnitude statistics applied to the Coso Geothermal field, *Geophys. Res. Lett.* **42**, no. 15, 6221–6228, doi 10.1002/2015GL064772.

Scholz, C. H. (1968). The frequency-magnitude relation of microfracturing in rock and its relation to earthquakes, *Bull Seism. Soc Am* **58**, no. 1, 399–415.

Schorlemmer, D., S. Wiemer, and M. Wyss (2005). Variations in earthquake-size distribution across different stress regimes, *Nature* **437**, no. 7058, 539–542, doi 10.1038/nature04094.

Shapiro, S. A., C. Dinske, C. Langenbruch, and F. Wenzel (2010). Seismogenic index and magnitude probability of earthquakes induced during reservoir fluid stimulations, *Lead. Edge* **29**, no. 3, 304–309.

Shi, Y., and B. A. Bolt (1982). The standard error of the magnitude-frequency b value, *Bull. Seismol. Soc. Am.* **72**, no. 5, 1677–1687, doi 10.1785/BSSA0720051677.

Stierle, E., V. Vavryčuk, J. Šílený, and M. Bohnhoff (2014). Resolution of non-double-couple components in the seismic moment tensor using regional networks—I: a synthetic case study, *Geophys. J. Int.* **196**, no. 3, 1869–1877, doi 10.1093/gji/ggt502.

Uski, M., and A. Tuppurainen (1996). A new local magnitude scale for the Finnish seismic network, *Seism. Source Parameters Microearthquakes Large Events* **261**, no. 1, 23–37, doi 10.1016/0040-1951(96)00054-6.

Uski, M., B. Lund, and K. Oinonen (2015). Scaling relations for homogeneous moment based magnitude, in *Evaluating Seismic Hazard for the Hanhikivi Nuclear Power Plant Site. Seismological Characteristics of the Seismic Source Areas, Attenuation of Seismic Signal, and Probabilistic Analysis of Seismic Hazard*, edited by J. Saari, B. Lund, M. Malm, P. Mäntyniemi, K. Oinonen, T. Tiira, M. Uski, and T. Vuorinen, p. 125 pp., Report NE-4459, ÅF-Consult Ltd.

Utsu (1965). A method for determining b in a formula log(N)=a-bM showing the magnitude-frequency distribution of earthquakes, *Geophys. Bull. Hokkaido Univ., Hokkaido, Japan* **13**, 99–103.

Utsu, T. (1961). A Statistical Study on the Occurrence of Aftershocks, *Geophys. Mag.* , no. 30, 521–605.

Verdecchia, A., E. S. Cochran, and R. M. Harrington (2021). Fluid-Earthquake and Earthquake-Earthquake Interactions in Southern Kansas, USA, Journal of Geophysical Research: Solid Earth 126, no. 3, e2020JB020384, doi 10.1029/2020JB020384.

Waldhauser, F., and W. L. Ellsworth (2000). A Double-Difference Earthquake Location Algorithm: Method and Application to the Northern Hayward Fault, California, *Bull Seism. Soc Am* **90**, no. 6, 1353–1368, doi 10.1785/0120000006.

Wang, L., G. Kwiatek, E. Rybacki, M. Bohnhoff, and G. Dresen (2020a). Injection-Induced Seismic Moment Release and Laboratory Fault Slip: Implications for Fluid-Induced Seismicity, *Geophys. Res. Lett.* **47**, no. 22, e2020GL089576, doi 10.1029/2020GL089576.

Wang, L., G. Kwiatek, E. Rybacki, A. Bonnelye, M. Bohnhoff, and G. Dresen (2020b). Laboratory study on fluid-induced fault slip behavior: The role of fluid pressurization rate, *Geophys. Res. Lett.* **47**, e2019GL086627, doi 10.1029/2019GL086627.

Weingarten, M., S. Ge, J. W. Godt, B. A. Bekins, and J. L. Rubinstein (2015). High-rate injection is associated with the increase in U.S. mid-continent seismicity, *Science* **348**, no. 6241, 1336–1340, doi 10.1126/science.aab1345.

Wiemer, S., and M. Wyss (2000). Minimum magnitude of completeness in earthquake catalogs: Examples from Alaska, the Western United States & Japan, *Bull Seism. Soc Am* **90**, 859–869, doi 10.1785/0119990114.

Ye, Z.-S., and N. Chen (2017). Closed-Form Estimators for the Gamma Distribution Derived From Likelihood Equations, *Am. Stat.* **71**, no. 2, 177–181, doi 10.1080/00031305.2016.1209129.

Yeo, I. W., M. R. M. Brown, S. Ge, and K. K. Lee (2020). Causal mechanism of injection-induced earthquakes through the Mw 5.5 Pohang earthquake case study, *Nat. Commun.* **11**, no. 1, 2614, doi 10.1038/s41467-020-16408-0.